

RTO WG 10: CFD Validation for Shock Wave Turbulent Boundary Layer Interactions

Doyle Knight* and Hong Yan[†]

*Rutgers - The State University of New Jersey
Mechanical and Aerospace Engineering
Piscataway, N.J. 08854-8058, USA*

*Argyris Panaras[‡]
Mechanical Engineering Department
National Technical University of Athens
Athens 15710, Greece*

*Alexander Zheltovodov[§]
Institute of Theoretical and Applied Mechanics
Siberian Branch of the Russian Academy of Sciences
Novosibirsk 630090, Russia*

NATO RTO Working Group 10 was established in December 1998 to examine the technologies of plug nozzles, scramjet propulsion and Computational Fluid Dynamics (CFD) for design of propelled hypersonic vehicles. The CFD subgroup evaluated six topics: boundary layer transition and instability, real gas flows, laminar viscous-inviscid interactions, shock-shock interactions, shock wave turbulent boundary layer interactions (SWTBLI) and base flows with and without plume interaction. This paper presents a summary of the evaluation of shock wave turbulent boundary layer interactions. Five configurations were considered: 2-D compression corner, 2-D expansion-compression corner, 2-D shock impingement, 3-D single fin and 3-D double fin. Recent Direct Numerical Simulations (DNS), Large Eddy Simulations (LES) and Reynolds-averaged Navier-Stokes (RANS) simulations are compared with experiment. The capabilities and limitations are described, and future research needs identified.

Nomenclature

c_f	Skin friction coefficient	τ	Shear stress
c_h	Heat transfer coefficient	μ	Dynamic molecular viscosity ($= \nu\rho$)
c_p	Pressure coefficient	aw	Adiabatic wall
k	Turbulence kinetic energy	c	Characteristic length
L	Length	DNS	Direct Numerical Simulation
ℓ	Turbulence length scale	E	Experiment
M	Mach number	LES	Large Eddy Simulation
p	Pressure	LES-D	Dynamic Smagorinsky model LES
Re	Reynolds number	LES-M	Monotone Integrated Large Eddy Simulation
T	Static temperature	LES-X	Mixed scale model LES
u, v, w	Cartesian velocity components	LES-S	Static Smagorinsky model LES
x, y, z	Cartesian coordinates	m	Mean value
u_τ	Wall friction velocity	RANS	Reynolds-averaged Navier-Stokes
α	Corner angle	SA	Spatial accuracy
δ	Boundary layer thickness	sep	Separation length
κ	Von Karman's constant	SS	Converged to steady state
ρ	Density	SWTBLI	Shock wave turbulent boundary layer interaction
		TA	Temporal accuracy
		TML	Throat middle line
		VD	Van-Driest transformation
		w	Wall
		∞	Upstream
		"	Favre-fluctuating component
		+	Normalized by ν_w/u_τ

*Professor, Department of Mechanical and Aerospace Engineering. Associate Fellow, AIAA.

[†]Research Associate, Department of Mechanical and Aerospace Engineering. Senior Member, AIAA.

[‡]Research Associate, Department of Mechanical Engineering. Associate Fellow, AIAA.

[§]Head, Separated Flows Research Group. Associate Fellow, AIAA.

Report Documentation Page

Form Approved
OMB No. 0704-0188

Public reporting burden for the collection of information is estimated to average 1 hour per response, including the time for reviewing instructions, searching existing data sources, gathering and maintaining the data needed, and completing and reviewing the collection of information. Send comments regarding this burden estimate or any other aspect of this collection of information, including suggestions for reducing this burden, to Washington Headquarters Services, Directorate for Information Operations and Reports, 1215 Jefferson Davis Highway, Suite 1204, Arlington VA 22202-4302. Respondents should be aware that notwithstanding any other provision of law, no person shall be subject to a penalty for failing to comply with a collection of information if it does not display a currently valid OMB control number.

1. REPORT DATE 01 JAN 2006	2. REPORT TYPE N/A	3. DATES COVERED -	
4. TITLE AND SUBTITLE RTO WG 10: CFD Validation For Shock Wave Turbulent Boundary Layer Interactions		5a. CONTRACT NUMBER	
		5b. GRANT NUMBER	
		5c. PROGRAM ELEMENT NUMBER	
6. AUTHOR(S)		5d. PROJECT NUMBER	
		5e. TASK NUMBER	
		5f. WORK UNIT NUMBER	
7. PERFORMING ORGANIZATION NAME(S) AND ADDRESS(ES) Rutgers The State University of New Jersey Mechanical and Aerospace Engineering Piscataway, NJ 08854-8058, USA		8. PERFORMING ORGANIZATION REPORT NUMBER	
9. SPONSORING/MONITORING AGENCY NAME(S) AND ADDRESS(ES)		10. SPONSOR/MONITOR'S ACRONYM(S)	
		11. SPONSOR/MONITOR'S REPORT NUMBER(S)	
12. DISTRIBUTION/AVAILABILITY STATEMENT Approved for public release, distribution unlimited			
13. SUPPLEMENTARY NOTES See also ADM001860, Technologies for Propelled Hypersonic Flight (Technologies des vols hypersoniques propulses). , The original document contains color images.			
14. ABSTRACT			
15. SUBJECT TERMS			
16. SECURITY CLASSIFICATION OF:			17. LIMITATION OF ABSTRACT
a. REPORT unclassified	b. ABSTRACT unclassified	c. THIS PAGE unclassified	UU
			18. NUMBER OF PAGES 30
			19a. NAME OF RESPONSIBLE PERSON

Introduction

Effective design of supersonic and hypersonic air vehicles requires accurate simulation methods for predicting aerothermodynamic loads (*i.e.*, mean and fluctuating surface pressure, skin friction and heat transfer). Shock wave turbulent boundary layer interaction (SWTBLI) is common in high speed flight, and can significantly affect the aerothermodynamic loads. The recent AGARD Working Group 18 (WG 18) study edited by Knight and Degrez¹ examined the capability of generalⁱ Reynolds-averaged Navier-Stokes (RANS) methods for prediction of 2-D and 3-D shock wave turbulent boundary layer interactions. The study comprised 13 configurations and 37 computations contributed by 18 participants. The recent review by Zheltovodov³ also examined the capability of RANS models for prediction of SWTBLI. Both studies concluded that general RANS methods accurately predicted mean surface pressure and heat transfer, and primary separation location for weak to moderateⁱⁱ 2-D and 3-D shock wave turbulent boundary layer interactions. For strong interactions, computed surface pressure and heat transfer distributions, and location of primary separation, show significant disagreement with experiment. In addition, the RANS calculations failed to capture the high level of unsteadiness in the shock system observed in the experiment and the appearance of secondary separation, and no RANS calculation provided a prediction of rms fluctuating surface pressure and heat transfer.

RTO Working Group 10 (WG 10) was established in December 1998 to examine three specific technologies for propelled hypersonic flight: plug nozzles (Subgroup 1), scramjet propulsion (Subgroup 2) and Computational Fluid Dynamics (Subgroup 3). Six specific topics were selected for evaluation by Subgroup 3 (Table 1) and specific experiments identified for CFD validation. A description of test cases was published.⁴ The test cases are also described in Knight.⁵

This paper presents the summary report of Topic No. 5, Shock Wave Turbulent Boundary Layer Interactions. Five separate configurations are considered. The 2-D compression corner (Fig. 1) and expansion-compression corner (Fig. 2) represent, for example, deflected aerodynamic control surfaces. The 2-D shock impingement (Fig. 3) typifies a shock boundary layer interaction within an inlet, for example. The 3-D single fin (Fig. 4) is typical of a fin-fuselage juncture. The 3-D double fin (Fig. 5) represents a sidewall compression inlet. All five configurations have been extensively studied and a substantial set of experimental data is available for each configuration.

ⁱBy *general* RANS method we mean a RANS model which has not been modified to take into account specific details of the flowfield structure. Significant progress has been made in development of *engineering* RANS methods which incorporate

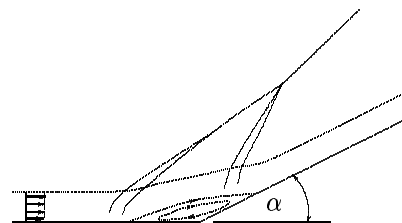


Fig. 1 2-D compression corner

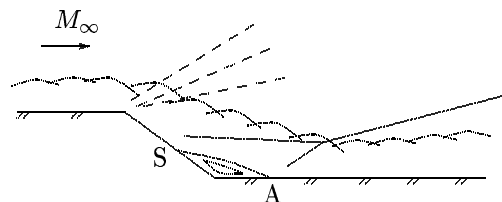


Fig. 2 2-D expansion-compression corner

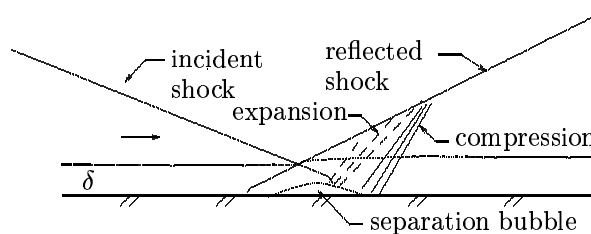


Fig. 3 2-D shock impingement

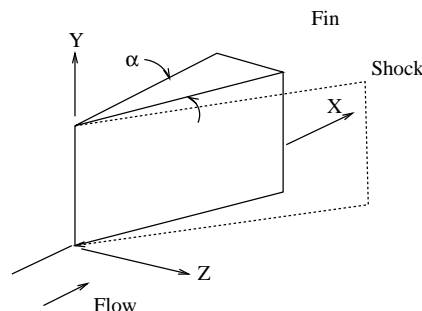


Fig. 4 3-D single fin

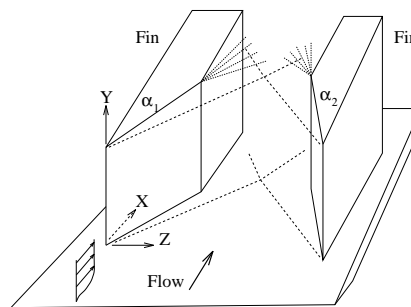


Fig. 5 3-D double fin

Contributions of recentⁱⁱⁱ numerical simulations for configuration-dependent flow physics. An example is Panaras.²

ⁱⁱIn this context, “weak” and “moderate” refer to the overall static pressure rise.

ⁱⁱⁱSimulations were selected from 1997 onward, since the review of Knight and Degrez¹ for AGARD WG 18 was completed

Table 1 Topics and Team Leaders

No.	Topic	Team Leader(s)
1	Boundary Layer Instability and Transition	Steven Schneider (Purdue University)
2	Real Gas Flows	Graham Candler (University of Minnesota)
3	Laminar Viscous-Inviscid Interactions	Michael Holden (CUBRC)
4	Shock-Shock Interactions	Steven Walker and John Schmisser (AFOSR)
5	Shock Wave-Turbulent Boundary Layer Interactions	Doyle Knight (Rutgers University)
6	Base Flows with and without Plume Interactions	Peter Bakker (Technical University of Delft) Phillipe Reijasse (ONERA)

the five cases were solicited through the RTO WG 10 membership and the RTO WG 10 website.⁶ The studies include Direct Numerical Simulation (DNS), Large Eddy Simulation (LES) and Reynolds-averaged Navier Stokes (RANS). The computed results are compared herein with the experimental data, and the overall capabilities of the CFD methods are assessed. Emphasis is placed on validation of the numerical methods, and therefore, in the interest of space, the description of the flowfield structures is intentionally limited.

2-D Compression Corner

The 2-D supersonic compression corner (Fig. 6) is a standard CFD validation case for shock wave turbulent boundary layer interactions. An equilibrium supersonic turbulent boundary layer approaches a compression corner defined by angle α . The deflection of the flow by the corner generates a shock system. For sufficiently large pressure rise, the boundary layer separates and a λ -shock forms. The shock system displays significant unsteadiness.⁷⁻¹⁰

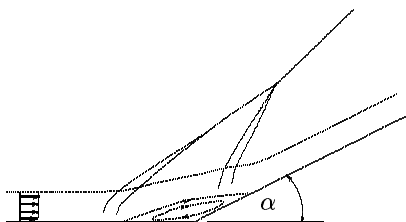


Fig. 6 2-D compression corner

An extensive number of analytical, computational, and experimental studies of the supersonic compression corner have been conducted. Recent reviews include Zheltovodov³ and Dolling.^{9,10} Earlier reviews include Green¹¹ and Delery.¹²

General RANS methods have failed to accurately predict the flowfield structure of the supersonic compression corner. Fig. 7 displays the computed mean separation length^{iv}, normalized by the characteristic length L_c proposed by Zheltovodov and Schülein^{13,14}

$$L_c = \frac{\delta}{M_\infty^3} \left(\frac{p_2}{p_{pl}} \right)^{3.1} \quad (1)$$

in early 1997.

^{iv}The mean separation length is the straight line distance between the mean separation and attachment points.

where δ is the upstream boundary layer thickness, M_∞ is the upstream freestream Mach number, p_2 is the downstream inviscid pressure, and p_{pl} is the plateau pressure computed according to the empirical formula by Zukoski¹⁵

$$p_{pl} = p_\infty \left(\frac{1}{2} M_\infty + 1 \right) \quad (2)$$

The solid lines define the limits of a large experimental database for supersonic compression corners over a wide range of Mach numbers. The RANS calculations are listed in Table 2. It is evident that RANS computations in general do not accurately predict the separation length.

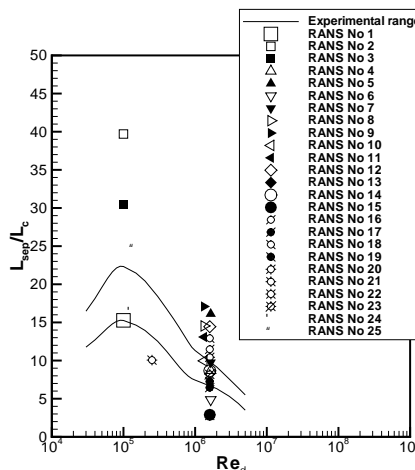


Fig. 7 Separation length for RANS

In the following sections, DNS and LES results are presented for several configurations. Mean quantities represent combined time and spanwise averages.

Case 1: Mach 3, $\alpha = 8^\circ$

Urbin *et al*²² simulated a Mach 3, $\alpha = 8^\circ$ compression corner at $Re_\delta = 2 \times 10^4$ and adiabatic wall conditions. Experimental data of Zheltovodov *et al*²³⁻²⁵ is available for $\alpha = 8^\circ$ at Reynolds numbers $Re_\delta = 7.5 \times 10^4$ and 1.1×10^5 . The flow conditions are summarized in Table 3. The inviscid pressure ratio across the shock $p_2/p_1 = 1.8$. As discussed in Zheltovodov,³ this configuration corresponds to an incipient intermittent separation. Although the mean flowfield is not separated, instantaneous reversed flow can exist for a short

Table 2 RANS calculations of 2-D Compression Corner

Number	Ref.	Model	α	Mach	$Re_\delta \times 10^{-6}$	L_{sep}/δ	L_{sep}/L_c
1	Shang ¹⁶	Equilibrium	25°	2.96	0.1	5.0	15.3
2	Shang ¹⁶	Frozen	25°	2.96	0.1	13.0	39.7
3	Shang ¹⁶	Relaxation	25°	2.96	0.1	10	30.5
4	Horstman ¹⁷	Baseline	20°	2.85	1.65	1.45	8.7
5	Horstman ¹⁷	Relaxation	20°	2.85	1.65	2.69	16.1
6	Horstman ¹⁷	Pressure Gradient	20°	2.85	1.65	0.81	4.87
7	Horstman ¹⁷	Relaxation+ Pressure Gradient	20°	2.85	1.65	1.62	9.75
8	Horstman ¹⁷	Baseline	24°	2.85	1.33	4.0	14.5
9	Horstman ¹⁷	Relaxation	24°	2.85	1.33	4.7	17.1
10	Horstman ¹⁷	Pressure Gradient	24°	2.85	1.33	2.74	9.96
11	Horstman ¹⁷	Relaxation+ Pressure Gradient	24°	2.85	1.33	3.6	13.1
12	Visbal,Knight ¹⁸	B-L	16°	2.9	1.6	1.0	14.4
13	Visbal,Knight ¹⁸	Modified B-L	16°	2.9	1.6	0.2	2.89
14	Visbal,Knight ¹⁸	Relaxation	16°	2.9	1.6	0.6	8.66
15	Visbal,Knight ¹⁸	Constant Ymax	16°	2.9	1.6	0.2	2.89
16	Visbal,Knight ¹⁸	B-L	20°	2.9	1.6	1.6	11.5
17	Visbal,Knight ¹⁸	Modified B-L	20°	2.9	1.6	0.9	6.46
18	Visbal,Knight ¹⁸	Relaxation	20°	2.9	1.6	1.8	12.9
19	Visbal,Knight ¹⁸	Modified B-L	24°	2.9	1.6	2.05	7.25
20	Visbal,Knight ¹⁸	Relaxation	24°	2.9	1.6	2.95	10.4
21	Ong,Knight ¹⁹	B-L	16°	1.96	0.25	2.15	10.1
22	Ong,Knight ¹⁹	B-L	16°	2.83	1.6	0.6	2.81
23	Ong,Knight ¹⁹	B-L	20°	2.83	1.6	1.75	8.19
24	Horstman ²⁰	$k - \varepsilon$	25°	3.0	0.133	4.89	16.3
25	Borisov <i>et al</i> ²¹	$k - \omega$	25°	3.0	0.139	7.38	24.8

time in the vicinity of the shock wave and near the wall due to the unsteadiness of the interaction process.

Table 3 Flow Conditions

Reference	Data	M_∞	$Re_\delta \times 10^{-4}$
Urbin <i>et al</i> ²²	LES	3.0	2.0
Zhel'tovodov <i>et al</i> ²³⁻²⁵	E	2.9	7.5 - 11

Details of the computation are presented in Table 4 where SA and TA indicate the spatial and temporal accuracy. An unstructured grid LES algorithm with a static Smagorinsky model was utilized. The inflow conditions were obtained from a separate computation of a flat plate adiabatic boundary layer at Mach 3. The inflow velocity profile satisfied the compressible Law of the Wall.²⁶ The inflow skin friction coefficient agreed with the empirical value obtained from the compressible Law of the Wall and Wake to within 6%, and the inflow adiabatic wall temperature was within 3% of the theoretical value obtained from the empirical formula

$$T_{aw} = T_\infty \left[1 + \frac{(\gamma-1)}{2} Pr_{t_m} M_\infty^2 \right] \quad (3)$$

where $Pr_{t_m} = 0.89$ is the mean turbulent Prandtl number.

Table 4 Details of Computations

Reference	Type	Cells	SA	TA
Urbin <i>et al</i> ²²	LES	1.6×10^6	2nd	2nd

An instantaneous image of the shock wave (as visualized by the isosurface $p/p_\infty = 1.25$) and the streamwise velocity at $y^+ = 10$ are shown in Fig. 8. Regions of negative velocity (instantaneous separation) are visible in qualitative agreement with the observations of Zhel'tovodov.³

The mean wall pressure distribution is shown in Fig. 9. The experimental profiles for the two different Reynolds numbers are essentially identical. The computed profile shows close agreement with experiment. The mean velocity profiles upstream and downstream of the corner are displayed in Fig. 10. The experimental data is for $Re_\delta = 1.1 \times 10^5$. The upstream profile is 3.3δ ahead of the corner and in the undisturbed flat plate boundary layer. The downstream profile is 3.5δ from the corner and located close to the position where the wall pressure reaches its asymptotic value. The computed results are in close agreement with experiment. The mean static temperature profiles at the same locations are shown in Fig. 11.

Upstream of the interaction the computed and experimental profiles are in close agreement. Downstream of the interaction, the profiles agree except within the region $0.05 \leq y/\delta \leq 0.25$ where the experimental value exceeds the prediction.

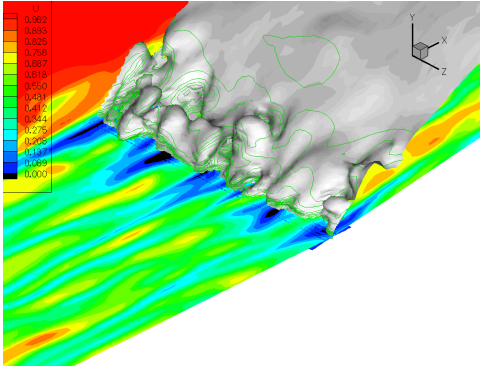


Fig. 8 Instantaneous velocity and shock

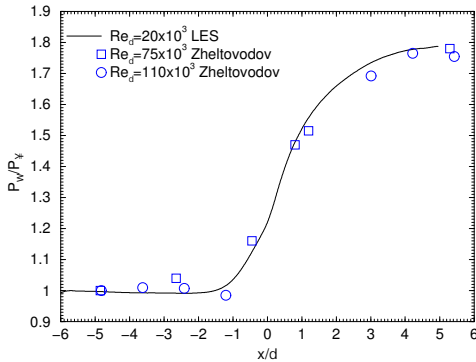


Fig. 9 Mean wall pressure

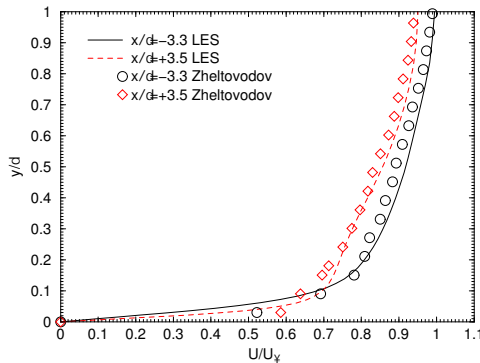


Fig. 10 Mean velocity

The Reynolds streamwise and shear stresses are displayed in Figs. 12 and 13, respectively, where the stresses have been normalized by the upstream wall shear stress τ_w . The experimental data of Muck *et al*²⁷ is shown. The experimental Reynolds number $Re_\delta = 1.6 \times 10^6$ is a factor of eighty greater than the LES. However, scaling of the Reynolds shear stress in a flat plate boundary layer by the wall shear stress τ_w has been shown to collapse the experimental data for a range of Mach and Reynolds numbers.²⁸ Thus,

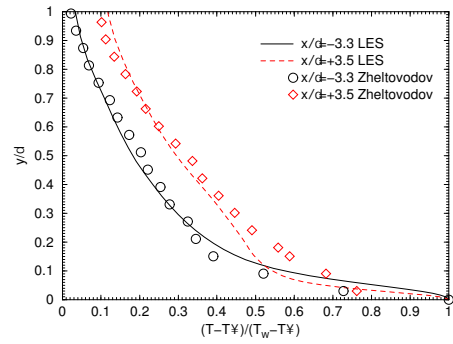


Fig. 11 Mean static temperature

the comparison of the LES and experiment is justified if only for qualitative comparison. The effect of the shock boundary layer interaction is to increase the level of Reynolds normal $\bar{\rho}u''u''$ and shear $\bar{\rho}u''v''$ stresses. The predicted values are in good agreement with experiment except for $y/\delta \leq 0.1$.

In summary, the following conclusions can be made:

- LES of the Mach 3, $\alpha = 8^\circ$ compression corner shows good agreement with the experimental mean surface pressure distribution and qualitatively correct modification of the mean velocity and turbulence profiles by the shock wave
- The mean flowfield is unseparated (and consequently, this case does not represent a particularly difficult case for LES), but the instantaneous flowfield indicates an incipient intermittent separation regime in accordance with the generalization of experimental data and analysis by Zheltovodov.³

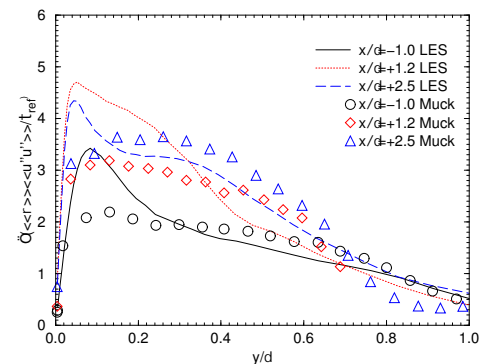


Fig. 12 Reynolds streamwise stress

Case 2: Mach 3, $\alpha = 18^\circ$

Adams²⁹⁻³¹ and Rizzetta *et al*³² simulated a Mach 3, $\alpha = 18^\circ$ compression corner at $Re_\delta = 2.1 \times 10^4$ and adiabatic wall conditions. No experimental data is available for this configuration. The inviscid pressure ratio across the shock is $p_2/p_1 = 3.37$.

Details of the computations are presented in Table 6. Adams performed a DNS. Rizzetta *et al* used three different approaches, namely, a DNS, an LES using a

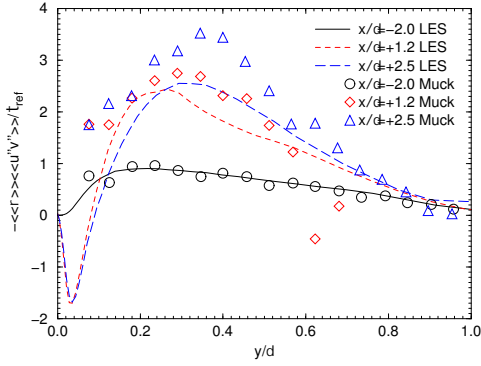


Fig. 13 Reynolds shear stress

Table 5 Flow Conditions

Reference	Data	M_∞	$Re_\delta \times 10^{-4}$
Adams ²⁹⁻³¹	DNS	3	2.1
Rizzetta <i>et al</i> ³²	DNS, LES	3	2.1

static Smagorinsky model for the SGS stresses (LES-s), and an LES using a dynamic (Germano *et al*³³) Smagorinsky model (LES-D). The inflow conditions were obtained in each instance from a separate computation of a flat plate adiabatic boundary layer at Mach 3 (Fig. 14).

Table 6 Details of Computations

Reference	Type	Grid	SA	TA
Rizzetta <i>et al</i> ³²	DNS	421 × 151 × 81	6th	2nd
	LES-S	421 × 151 × 81	6th	2nd
	LES-D	421 × 151 × 81	6th	2nd
Adams ²⁹⁻³¹	DNS	1000 × 180 × 80	5th	3rd

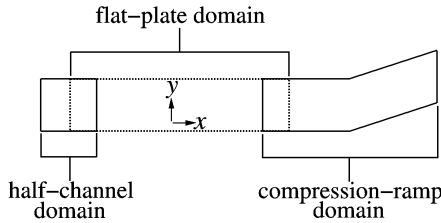


Fig. 14 Generation of inflow conditions

Although the Mach number and Reynolds number were nominally identical, the inflow profiles differ significantly. Figs. 15 and 16 display the mean and rms fluctuating streamwise velocity at the inflow boundary (“present” indicates the results of Rizzetta *et al*). Major differences are evident, and have a significant effect on the computed shock boundary layer interaction.

The computed mean surface pressure coefficient $c_p = (p - p_\infty) / \frac{1}{2} \rho_\infty U_\infty^2$ is shown in Fig. 17. The size of the interaction region, defined by the location of the initial rise in c_p and intersection of c_p with the downstream inviscid value ($c_p = 0.376$), is substantially larger in the simulation of Adams compared to Rizzetta. This is attributable to the differences in the inflow velocity profile (Fig. 15), as the momentum flux ρu is lower near the wall in Adams’ profile (see also

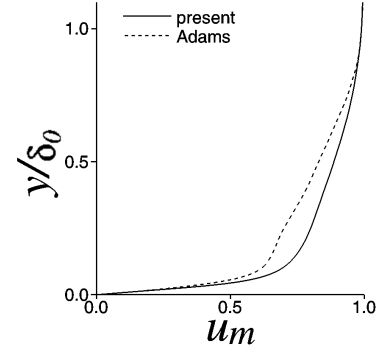


Fig. 15 Inflow mean velocity

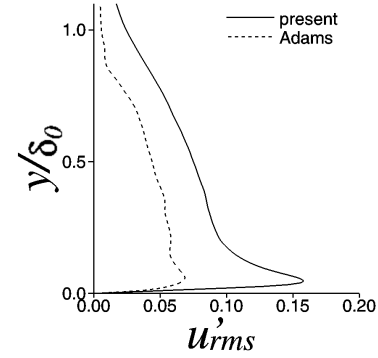


Fig. 16 Inflow rms streamwise velocity

Fig. 20). The DNS and LES profiles of Rizzetta are virtually identical, implying the SGS model has negligible effect.

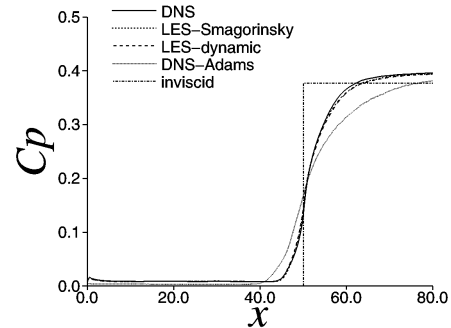


Fig. 17 Mean surface pressure

The computed mean skin friction coefficient $c_f = \tau_w / \frac{1}{2} \rho_\infty U_\infty^2$ is shown in Fig. 18. The upstream skin friction level is virtually identical for both Adams and Rizzetta (see Fig. 15 which indicates the velocity profiles are essentially the same within the viscous sub-layer). The separation length predicted by Adams is approximately 130% larger than Rizzetta. This is attributable to the lower momentum flux in the incoming boundary layer (Fig. 15). The DNS and LES profiles of Rizzetta are virtually identical, again indicating the SGS model has negligible effect.

The mean velocity and static temperature are displayed in Figs. 19 and 20, respectively. Station Nos. 1, 2 and 3 are located upstream of the interaction re-

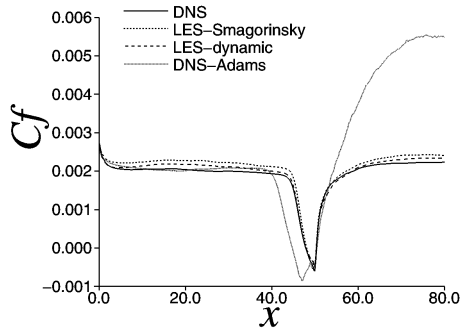


Fig. 18 Mean skin friction

gion, at the corner, and downstream of the corner, respectively. The mean velocity profiles are displayed using the Van Driest³⁴ transformation. All profiles exhibit agreement with the Law of the Wall logarithmic profile in the region $20 \leq y^+ \leq 100$ (Station No. 1). Downstream of the corner, the simulations by Rizzetta show recovery of the near wall region to the equilibrium Law of the Wall, while the simulation by Adams does not. Significant differences in the mean temperature between Adams and Rizzetta are evident both upstream, at and downstream of the corner. These are associated with differences in the mean velocity, since the total temperature is approximately constant across the boundary layer. For both the velocity and temperature profiles, the DNS and LES results of Rizzetta are virtually identical.

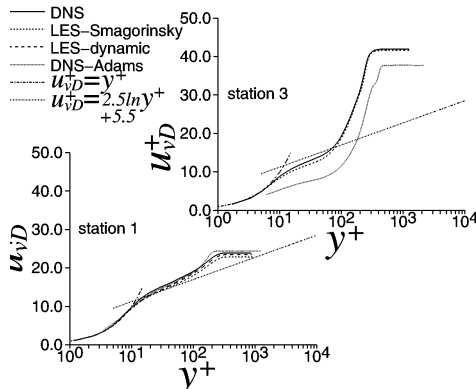


Fig. 19 Mean velocity

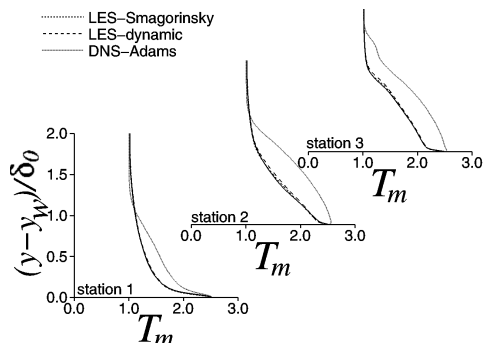


Fig. 20 Mean static temperature

Spanwise turbulent kinetic energy spectra at two separate positions within the boundary layer and three streamwise locations are shown in Figs. 21 and 22 where the location is defined in terms of the inflow boundary layer condition. All curves have been normalized to unity at $k_3 = 1$. The results of Rizzetta are consistently higher than Adams, implying a higher level of turbulent kinetic energy. This result is confirmed by comparison of profiles for the streamwise, normal vertical and spanwise rms fluctuating velocities.³² The profiles of Rizzetta display the emergence of an inertial subrange ($E(k) \propto k^{-5/3}$). The inertial subrange properly occurs at wavenumbers above the peak in the energy spectrum.³⁵ Adams' results do not display an inertial subrange. The spectra of Rizzetta at high wavenumber show higher energy for the LES than DNS calculations. This is an unexplained result, since it would be expected that the SGS model would dissipate more energy at higher wavenumber than the DNS.

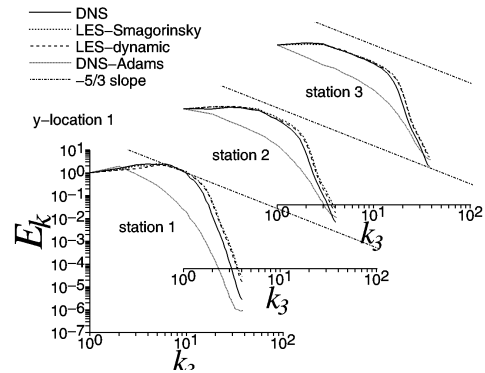


Fig. 21 Spanwise TKE spectra at $y^+ = 7.3 (y/\delta = 0.034)$

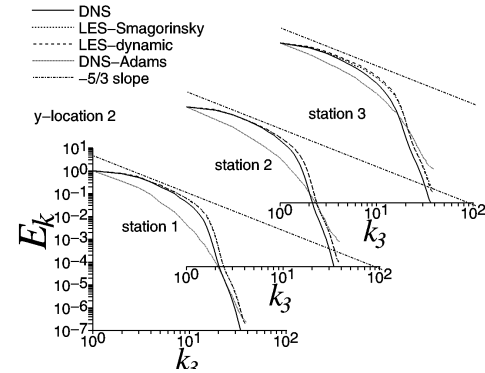


Fig. 22 Spanwise TKE spectra at $y^+ = 132 (y/\delta = 0.61)$

The computed separation length, normalized using (1), is shown in Fig. 23. The computed separation lengths of Rizzetta are below the linear extrapolation of the lower bound of the experimental band, while the computed separation length of Adams lies above the upper bound.

In summary, the following conclusions may be made:

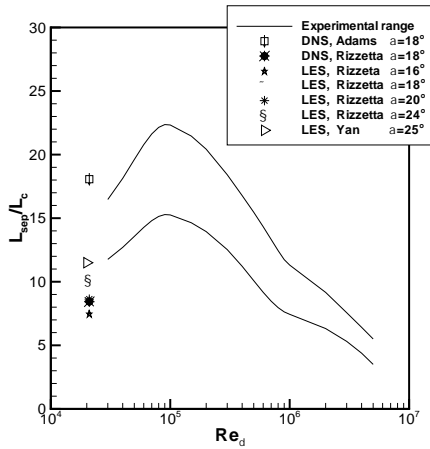


Fig. 23 Separation length for DNS and LES

- DNS of shock wave turbulent boundary layer interactions is sensitive to the inflow profiles
- The DNS and LES of Rizzetta are virtually identical for all profiles. This implies that the SGS model has a negligible effect.
- The computed mean separation lengths are outside the linear extrapolation of the experimental data

Case 3: Mach 3, $\alpha = 24^\circ$

Rizzetta and Visbal³⁶ simulated a Mach 3, $\alpha = 24^\circ$ compression corner at $Re_\delta = 2.1 \times 10^4$ and adiabatic wall conditions^v. Experimental data is available from Settles *et al.*,³⁷ Dolling and Murphy³⁸ and Smits and Muck³⁹ as indicated in Table 7^{vi}. However, the Reynolds number for the experiment is significantly higher than the simulation by a factor of 40 to 77. Therefore, the comparison between simulation and experiment is qualitative. The inviscid pressure ratio across the shock is $p_2/p_1 = 4.68$.

Table 7 Flow Conditions

Reference	Data	M_∞	$Re_\delta \times 10^{-6}$
Rizzetta <i>et al.</i> ³⁶	LES	3.0	.021
Settles <i>et al.</i> ³⁷	E	2.84 – 2.87	1.5 – 1.6
Dolling <i>et al.</i> ³⁸	E	2.90 – 2.95	0.81 – 1.4
Smits <i>et al.</i> ³⁹	E	2.79 – 2.87	1.6

Details of the computation^{vii} are presented in Table 8. A structured grid LES algorithm using a dynamic Smagorinsky model was utilized.

The effect of the difference in Reynolds number is evident in the inflow profiles of streamwise velocity

^vRizzetta and Visbal³⁶ also simulated $\alpha = 8^\circ, 16^\circ$ and 20° at $Re_\delta = 2.1 \times 10^4$.

^{vi}Please note that the reference numbers in Figs. 24 to 32 correspond to the references in Rizzetta and Visbal.³⁶

^{vii}A coarse grid simulation ($211 \times 76 \times 81$) was also performed which demonstrated that the fine grid solution for the surface pressure was grid converged.

Table 8 Details of Computations

Reference	Type	Grid	SA	TA
Rizzetta <i>et al.</i> ³⁶	LES	$421 \times 151 \times 181$	6th	2nd

(Fig. 24), streamwise Reynolds stress (Fig. 25) and Reynolds shear stress (Fig. 26). The computed inflow mean velocity is lower than the experiment near the wall as expected.

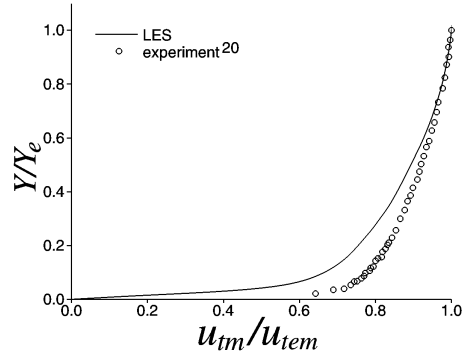


Fig. 24 Inflow velocity

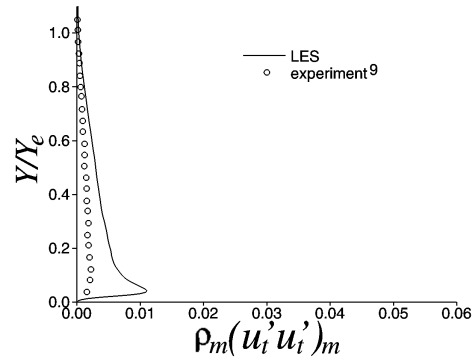


Fig. 25 Inflow Reynolds streamwise stress

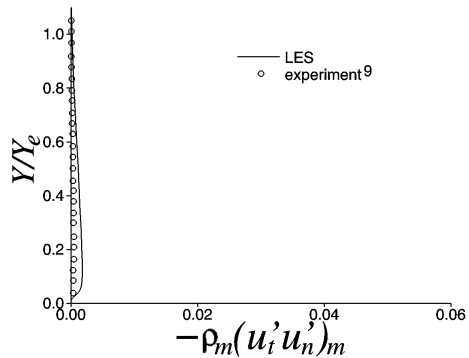


Fig. 26 Inflow Reynolds shear stress

The mean wall pressure is shown in Fig. 27. The upstream influence, plateau and recovery regions are accurately predicted, notwithstanding the difference in Reynolds number between the simulation and ex-

periment. The standard deviation σ_p of the surface pressure fluctuations, normalized by the local mean wall pressure p_w , is displayed in Fig. 28. The experimental³⁸ peak value is associated with the fluctuating motion of the separation shock. The simulation significantly underestimates the peak value, and overestimates the level of fluctuations downstream of the corner. Similarly, Fig. 29 indicates that the simulation underestimates the peak value of skewness $S = \overline{p'^3}/\sigma_p^3$ near separation. These discrepancies can be understood by considering the time history of the surface pressure fluctuations in the experiment and simulation. Fig. 30 shows a time history of the surface pressure at midspan and $x/\delta = -2.1$ which is near the location of the peak values of the standard deviation (Fig. 28) and skewness (Fig. 29). The experiment displays a high intermittency of the pressure signal associated with low frequency motion of the separation shock. The simulation displays no low frequency component.

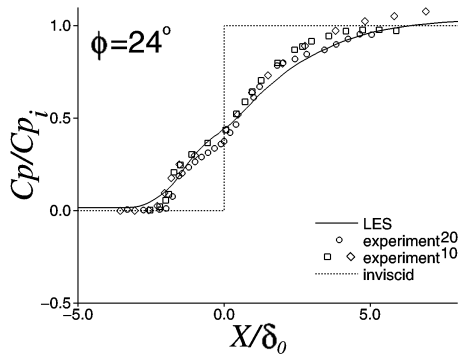


Fig. 27 Mean wall pressure

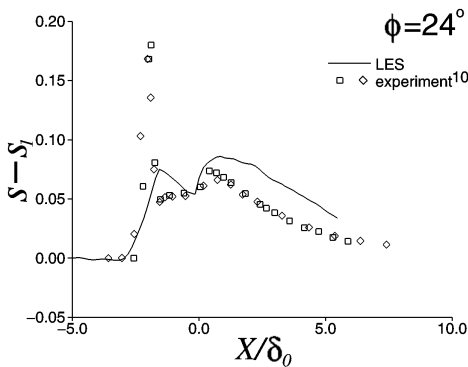


Fig. 28 Standard deviation of wall pressure

The mean skin friction coefficient is shown in Fig. 31. The position of separation and reattachment (as measured from the corner at $x = 0$) are significantly overestimated, and the recovery of the skin friction downstream of attachment substantially underpredicts the experiment.

The computed separation length, normalized using (1), is shown in Fig. 23. The computed separation

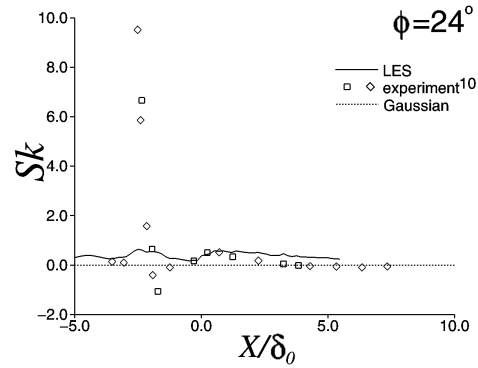


Fig. 29 Skewness of wall pressure

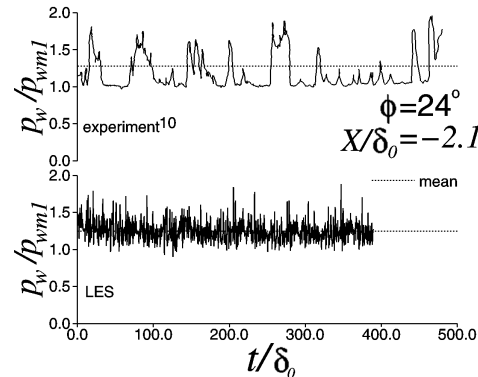


Fig. 30 Time history of wall pressure

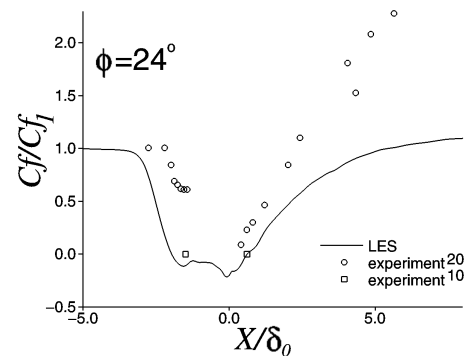


Fig. 31 Mean skin friction

length is at the lower limit of a linear extrapolation of the experimental band.

Velocity profiles at two locations downstream of the corner at $x/\delta = 1.33$ and 2.65 are displayed in Fig. 32. The underestimate in the velocity in the near wall region is consistent with the comparison of computed and experimental upstream profiles (Fig. 24).

In summary, the following conclusions can be made:

- The mean surface pressure shows good agreement with experiment. This may be fortuitous, however, in view of the significant difference in Reynolds number between the simulation and experiment, and the substantial differences in surface pressure fluctuation statistics in the vicinity

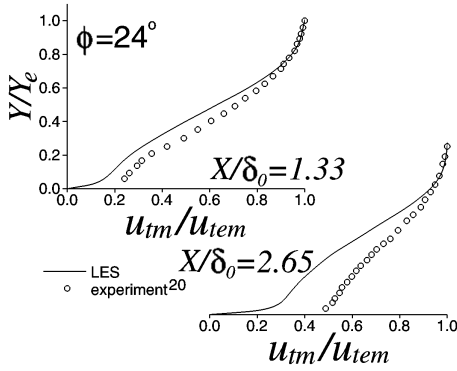


Fig. 32 Velocity profiles

of separation.

- The computed separation length is at the lower limit of the experimental data correlation.
- The near wall velocity profiles downstream of the corner are significantly underpredicted, likely due to the difference in inflow profiles associated with the disparity in Reynolds numbers.

Case 4: Mach 3, $\alpha = 25^\circ$

Yan *et al*⁴⁰ simulated a Mach 2.88, $\alpha = 25^\circ$ compression corner at $Re_\delta = 2 \times 10^4$ and adiabatic wall conditions. Experimental data of Zheltovodov *et al*^{3, 23–25, 41} is available for $\alpha = 25^\circ$ at Reynolds number $Re_\delta = 6.4 \times 10^4$. The flow conditions are summarized in Table 9. The inviscid pressure ratio across the shock $p_2/p_1 = 4.7$. The mean flowfield is separated at the corner.

Table 9 Flow Conditions

Reference	Data	M_∞	$Re_\delta \times 10^{-4}$
Yan <i>et al</i> ⁴⁰	LES	2.88	2.0
Zheltovodov <i>et al</i> ^{3, 23–25, 41}	E	2.88	6.4

Details of the computation are presented in Table 10. An unstructured grid LES algorithm using the MILES model⁴² was utilized. In the MILES model, the inherent dissipation in the numerical algorithm constitutes the SGS model. The inflow velocity profile satisfied the Law of the Wall. The inflow skin friction coefficient agreed with the empirical value obtained from the compressible Law of the Wall and Wake to within 6%. The inflow adiabatic wall temperature was within 3% of the theoretical value obtained from (3).

Table 10 Details of Computations

Reference	Type	Cells	SA	TA
Yan <i>et al</i> ⁴⁰	LES	2.0×10^6	2nd	2nd

The mean wall pressure is shown in Fig. 33^{viii}. The upstream influence (*i.e.*, the location of the initial

^{viii}The reference number for the experiment in Figs. 33 and 34 correspond to the references listed in Yan *et al*.⁴⁰

pressure rise) is accurately predicted; however, the computed pressure distribution does not show the distinct plateau evident in the experiment, and recovers to the downstream inviscid pressure more rapidly than the experiment.

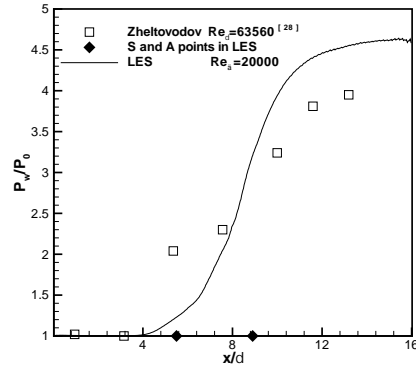


Fig. 33 Mean wall pressure

The mean skin friction coefficient is shown in Fig. 34. The initial drop in skin friction associated with the adverse pressure gradient is reasonably predicted. The predicted recovery of the skin friction downstream of reattachment is more rapid than in the experiment, similar to the results for the surface pressure.

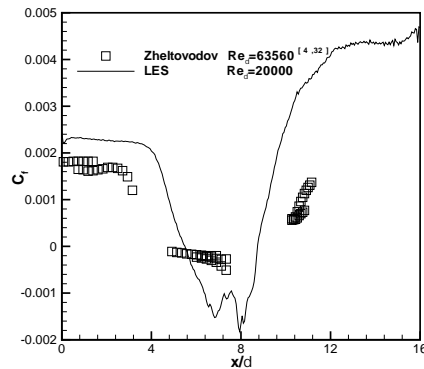


Fig. 34 Mean skin friction coefficient

The computed mean separation length is shown in Fig. 23. The value lies within a linear extrapolation of the band of experimental data.

Fig. 35 displays the instantaneous shock wave structure defined by an isosurfaces of static pressure at $p/p_\infty = 1.4$ and 2.0, together with the contours of the streamwise velocity at $y^+ = 7$. The λ shock is consistent with the experimental Schlieren image (Fig. 36).

In summary, the following conclusions can be made:

- The LES does not accurately reproduce the mean surface pressure. This may be attributable to the difference in Reynolds numbers between the LES and experiment.

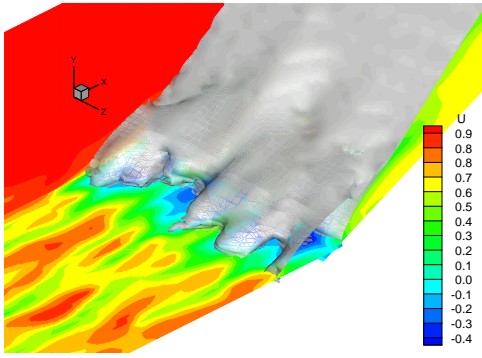


Fig. 35 Instantaneous shock structure

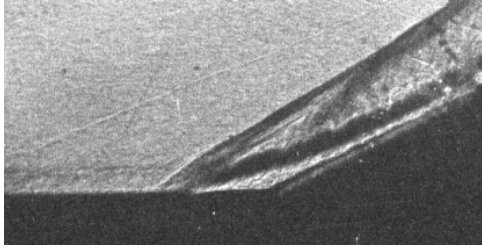


Fig. 36 Schlieren image

- The LES predicts a mean separation length consistent with a linear extrapolation of the experimental data.

2-D Expansion-Compression Corner

The expansion-compression corner (Fig. 37) provides a test of modeling of shock wave turbulent boundary layer interaction wherein the incoming boundary layer is non-equilibrium. An initially equilibrium supersonic turbulent boundary layer is expanded through an angle α and subsequently compressed through the same angle. The expansion reduces the turbulence kinetic energy and increases the mean kinetic energy within the boundary layer.

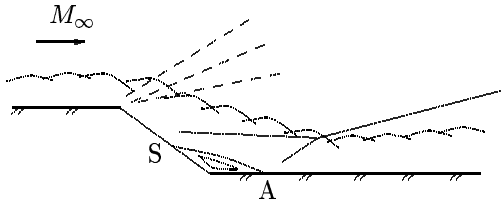


Fig. 37 Expansion-compression corner

In the following section, an LES of the expansion-compression corner is presented. Mean quantities represent combined time and spanwise averages.

Case 1: Mach 3, $\alpha = 25^\circ$

Yan *et al*⁴³ simulated a Mach 2.88 expansion compression corner at $Re_\delta = 2 \times 10^4$ and adiabatic wall conditions. Experimental data of Zheltovodov *et al*^{13, 14, 25, 44-48} is available for $\alpha = 25^\circ$ at $M_\infty = 2.9$ and $Re_\delta = 4.1 \times 10^4$ to 1.95×10^5 . The flow conditions are shown in Table 11. The inviscid pressure ratio across the expansion is $p_2/p_1 = 0.098$, and the Mach

number downstream of the expansion is $M_2 = 4.59$. Across the subsequent compression, the pressure ratio is $p_3/p_2 = 8.60$ and the downstream Mach number $M_3 = 2.43$.

Table 11 Flow Conditions

Reference	Data	M_∞	$Re_\delta \times 10^{-4}$
Yan <i>et al</i> ⁴³	LES	2.88	2.0
Zheltovodov ^{13, 14, 25, 44-48}	E	2.88	4.4 – 50.

Details of the computation are presented in Table 12. An unstructured grid LES algorithm using the MILES model⁴² was utilized. The inflow profile is the same as Case 1 of the 2-D compression corner.

Table 12 Details of Computations

Reference	Type	Cells	SA	TA
Yan <i>et al</i> ⁴³	LES	2.4×10^6	2nd	2nd

The computed flowfield structure is shown in Figs. 38 and Fig. 39 which display the mean static pressure and streamlines (s is separation, A is attachment). The flow expands around the first corner, and recompresses at the second corner. The shock wave turbulent boundary layer at the second corner is sufficiently strong to separate the boundary layer as evident in Fig. 39. The flowfield structure is in good agreement with the results of Zheltovodov and his colleagues^{3, 13, 14, 25, 45, 47, 48} which are shown qualitatively in Fig. 37.

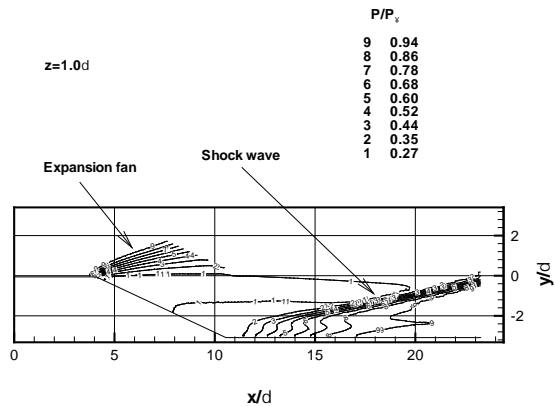


Fig. 38 Mean static pressure

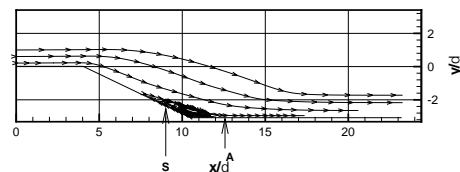


Fig. 39 Mean streamlines

Mean velocity profiles in the x -direction are shown in Fig. 40 at $x = 2\delta$ and $x = 6\delta$, where x is measured from the inflow along the direction of the inflow freestream velocity (Fig. 38). The abscissa is the component of velocity locally parallel to the wall, and the ordinate is the distance measured normal to the wall. The first profile is upstream of the expansion corner (which is located at $x = 4\delta$). The second profile is downstream of the expansion fan and upstream of the separation point. The computed mean velocity profile at the first location is slightly fuller than the experiment. This is consistent with the experimentally observed dependence of the exponent n in the power-law $U/U_\infty = (y/\delta)^{1/n}$ on the Reynolds number. The second profile shows a significant acceleration of the flow in the outer portion of the boundary layer due to the expansion.

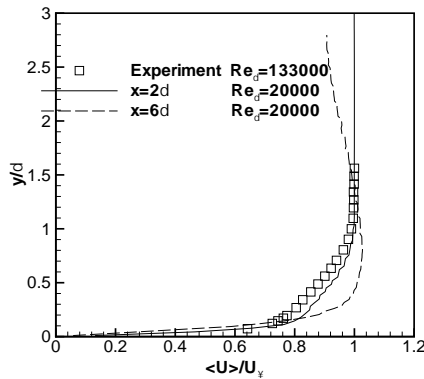


Fig. 40 Mean velocity

The surface pressure is displayed in Fig. 41. The surface pressure drops rapidly at the first corner. The shock boundary layer interaction at the second corner causes separation of the boundary layer and a concomitant plateau in the surface pressure.⁴⁹ The experiments display an increase in the size of the pressure plateau region with decreasing Reynolds number. The computed results for $Re_\delta = 2 \times 10^4$ are in good agreement with the experimental data at the lowest Reynolds number ($Re_\delta = 4.1 \times 10^4$) for the location, extent and magnitude of the pressure plateau. Also, the shape of the experimental pressure plateau shows little variation for $Re_\delta \leq 6.8 \times 10^4$, thus suggesting that the computed pressure plateau region (for $Re_\delta = 2 \times 10^4$) is accurate. The computed recovery of the surface pressure is more rapid than in the experiment, however.

The computed and experimental mean skin friction coefficient $c_f = \tau_w / \frac{1}{2} \rho_\infty U_\infty^2$ are shown in Fig. 42. The skin friction coefficient increases rapidly downstream of attachment. The computed results at $Re_\delta = 2 \times 10^4$ are in close agreement with the experimental data at $Re_\delta = 8.0 \times 10^4$ and 1.94×10^5 in the region downstream of reattachment.

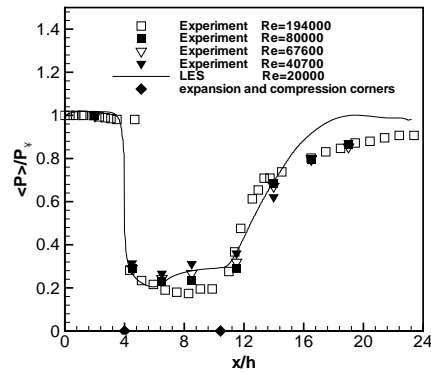


Fig. 41 Surface pressure

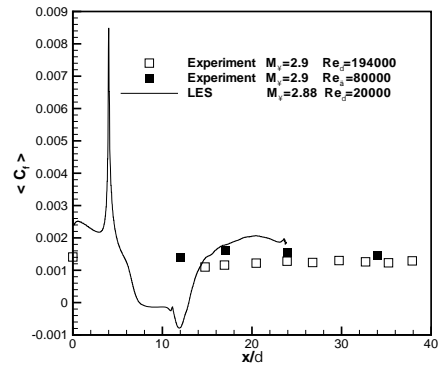


Fig. 42 Skin friction coefficient

Zhel'tovodov and Schülein¹³ has correlated experimental data for the scaled separation length L_{sep}/L_c defined by (1) for the expansion-compression corner where δ_e is the incoming boundary layer thickness (upstream of the expansion corner), p_2 is the pressure after the shock in inviscid flow, p_{pl} is the plateau pressure from the empirical formula of Zukoski¹⁵ $p_{pl} = p_e(\frac{1}{2}M_e + 1)$ where p_e and M_e are the static pressure and freestream Mach number upstream of the compression corner and downstream of the expansion fan. In the computation, the location is taken to be $x = 6\delta$. The values of M_e and p_2 have been computed using inviscid theory. Also, $Re_{\delta_e} = 1.8 \times 10^4$ for LES ($Re_{\delta_e} = \rho_e U_e \delta_e / \mu_e$, where ρ_e , U_e and μ_e are computed using inviscid theory). The experimental data correlation and the computed result⁴³ for the scaled separation length is shown in Fig. 43. The computed value is consistent with a linear extrapolation of the experimental data.

In summary, the following conclusions can be made:

- The LES accurately reproduces the mean surface pressure and rapid recovery of the skin friction downstream of attachment to a level close to the undisturbed upstream in agreement with experiment

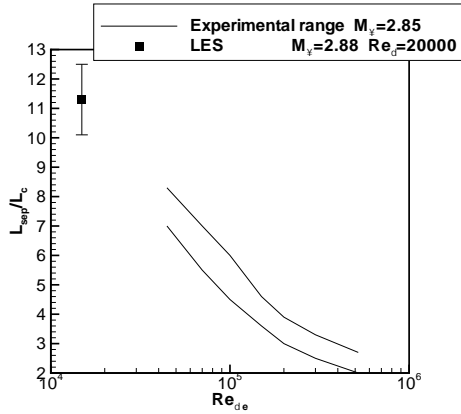


Fig. 43 Separation length

- The LES predicts a mean separation length consistent with a linear extrapolation of the experimental data

2-D Shock Impingement

The shock impingement (Fig. 44) is analogous to the 2-D compression corner (Fig. 1). An incident shock, generated by a wedge of angle α , interacts with an equilibrium supersonic turbulent boundary layer. For sufficiently large pressure rise, the boundary layer separates and a system of shock waves and expansions form. The mean surface pressure distribution is similar to the 2-D compression corner at the same overall pressure rise.¹² Reviews are presented in Green¹¹ and Delery.¹²

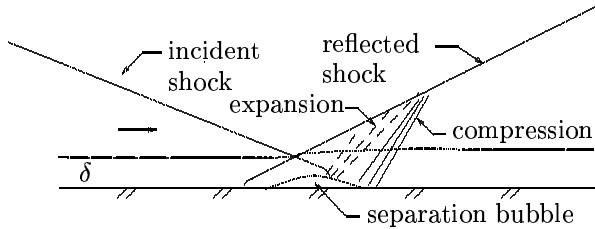


Fig. 44 2-D shock impingement

Case 1: Mach 2.3, $\alpha = 8^\circ$

Garnier *et al*^{50,51} simulated a Mach 2.3 impinging shock at $Re_\delta = 6.0 \times 10^4$. The incident shock angle is 32.4° corresponding to a wedge angle $\alpha = 8^\circ$. The wall is adiabatic. Experimental data of Deleuze⁵² and Laurent⁵³ is available. The flow conditions are summarized in Table 13. The overall inviscid pressure ratio across the shocks $p_2/p_1 = 2.47$.

Table 13 Flow Conditions

Reference	Data	M_∞	$Re_\delta \times 10^{-4}$
Garnier <i>et al</i> ^{50,51}	LES	2.3	6.0
Deleuze, ⁵² Laurent ⁵³	E	2.3	6.0

Details of the computation are presented in Table 14. A structured grid LES algorithm was utilized. Three computations (denoted by LES-X (A)

to LES-X (C)) were performed using the Mixed Scale Model,⁵⁴⁻⁵⁶ and one computation using MILES (denoted by LES-M (D)). The inflow conditions were obtained from a separate computation of a flat plate adiabatic boundary layer. The inflow velocity satisfies the compressible Law of the Wall as indicated in Fig. 45 where HWA indicates the experimental data obtained using Hot Wire Anemometry.

Table 14 Details of Computations

Reference	Type	Grid	SA	TA
Garnier ^{50,51}	LES-X (A)	$255 \times 55 \times 151$	2nd	2nd
	LES-X (B)	$255 \times 110 \times 151$	2nd	2nd
	LES-X (C)	$510 \times 55 \times 151$	2nd	2nd
	LES-M (D)	$510 \times 55 \times 151$	2nd	2nd

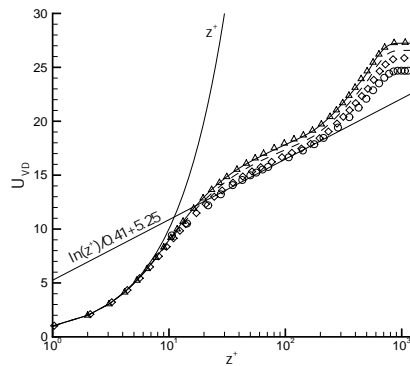


Fig. 45 Velocity (A —, B Δ , C ---, D \diamond , HWA \circ)

The mean skin friction coefficient is shown in Fig. 46. The computations using the Mixed Scale Model are in close agreement with experiment and each other. The MILES computation (Case D) also displays close agreement with experiment, and exhibits a smaller separation region (consistent with higher inflow turbulence level near the wall^{50,51}).

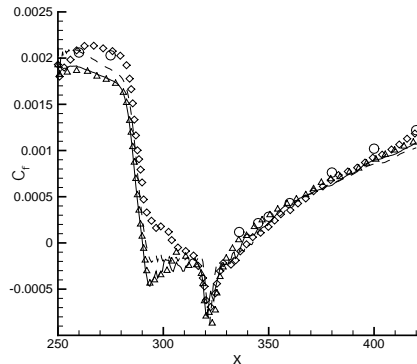


Fig. 46 Skin friction (A —, B Δ , C ---, D \diamond , HWA \circ)

The evolution of the compressible displacement thickness δ_1 is displayed in Fig. 47. All computations

shown good agreement with experiment within the interaction region, although overestimating δ_1 in the recovery region downstream by approximately 10%.

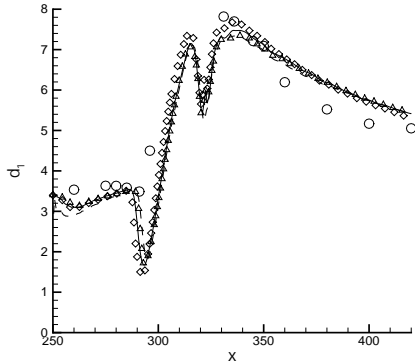


Fig. 47 Displacement thickness (A —, B Δ , C ---, D \diamond , HWA \circ)

The mean streamwise velocity profiles at $x = 351$ mm (computations) and $x = 345$ mm (experiment) are shown in Fig. 48 where LDA indicates the experimental measurements using Laser Doppler Anemometer. An additional profile for Case A is shown at $x = 345$ mm. The x location is immediately downstream of reattachment (Fig. 46). Note the velocity is the ordinate and the distance from the wall (normalized by the incoming boundary layer thickness) is the abscissa. The offset between the x locations for the computations and experiment accounts for the apparent displacement of the incident shock in the computations. The overall agreement between computation and experiment is good.

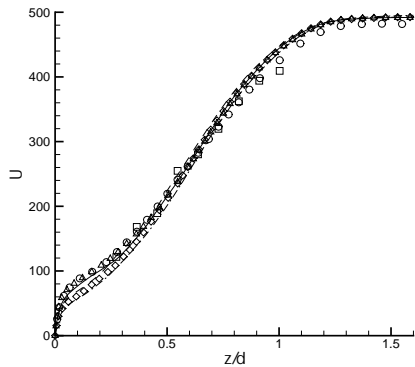


Fig. 48 Velocity (A ($x = 351$ mm) —, A ($x = 345$ mm) - \bullet -, B Δ , C ---, D \diamond , HWA \circ , LDA \square)

The rms streamwise fluctuating velocity profiles at $x = 326$ mm (computations) and $x = 320$ mm (experiment) are shown in Fig. 49, and at $x = 351$ mm (computations) and $x = 345$ mm (experiment) in Fig. 50. An additional profile for Case A is shown at $x = 320$ mm and $x = 345$ mm in Figs. 49 and 50, respectively. The profiles in Fig. 49 correspond

to the separated region, and the profiles in Fig. 50 are located downstream of the reattachment of the boundary layer (Fig. 46). In Fig. 49, the computed profiles display general agreement with experiment (LDA). In Fig. 50, there is a significant difference between the HWA and LDA measurements especially in the middle of the boundary layer. The computations show good agreement with the LDA data.

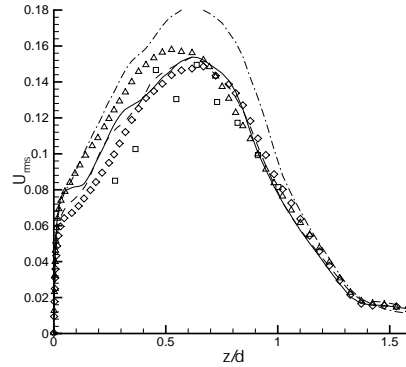


Fig. 49 Rms velocity (A ($x = 326$ mm) —, A ($x = 320$ mm) - \bullet -, B Δ , C ---, D \diamond , LDA \square)

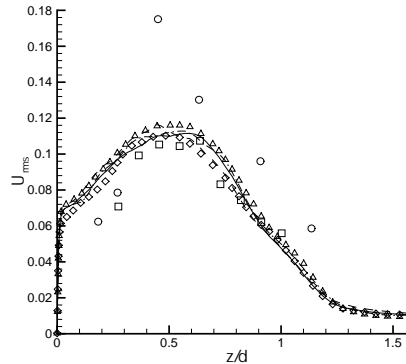


Fig. 50 Rms velocity (A ($x = 351$ mm) —, A ($x = 345$ mm) - \bullet -, B Δ , C ---, D \diamond , HWA \circ , LDA \square)

In summary, the following conclusions can be made:

- The LES accurately predicts the displacement thickness, skin friction coefficient, and velocity profiles
- The LES shows reasonable agreement with the LDA measurements of rms streamwise turbulent fluctuations
- The differences between the Mixed Model and MILES results are small

3-D Single Fin

The 3-D single fin (Fig. 51) is a standard CFD validation case for shock wave turbulent boundary layer interaction. An equilibrium supersonic turbulent boundary layer approaches a semi-infinite fin of angle α . The deflection of the flow by the fin generates a swept shock system. For a sufficiently large pressure rise, the boundary layer separates and a λ -shock forms. The flowfield structure is well understood.^{3, 57–65}

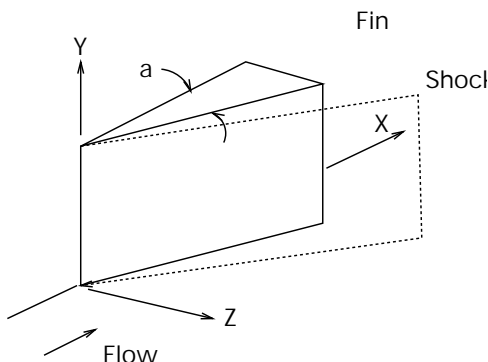


Fig. 51 3-D single fin

Zheltovodov *et al*^{57, 58, 60} identified six regimes for the 3-D single fin flowfield depending on the strength of the shock wave. Fig. 52 displays the surface streamline patterns for each of the regimes^{ix}. In Regime I, the boundary layer is unseparated and no convergence of surface streamlines is observed. In Regime II, the streamlines turn approximately parallel to the inviscid shock but do not form a line of coalescence. In Region III, a primary separation line (S_1) forms corresponding to the coalescence of the surface streamlines. An attachment line (R_1) forms near the fin-plate juncture. A line of secondary separation (S_2) appears located between the primary separation (S_1) and attachment (R_1) lines. In Regimes IV to VI, the secondary separation (S_2) and attachment (R_2) lines disappear and finally reappear.

General RANS models are capable of predicting the primary features of the flowfield including the wall pressure distribution (albeit with some notable errors for strong interactions), and location of separation and attachment lines. However, the skin friction distribution is not accurately predicted^x for strong interactions.^{1, 3, 62} Moreover, the phenomenon of the appearance/disappearance/re-appearance of secondary separation has not been previously predicted.⁶¹

Cases 1-3: Mach 3, $\alpha = 15^\circ$ and Mach 4, $\alpha = 20^\circ$ and 30.6°

Thivet⁶⁶ simulated three different configurations of the 3-D single fin. The flow conditions are listed in Table 15. Experimental data of Zheltovodov *et al*^{57, 58}

^{ix}SW identifies the trace of the inviscid shock.

^xA notable exception is the prediction of the modified Baldwin-Lomax model by Panaras.²

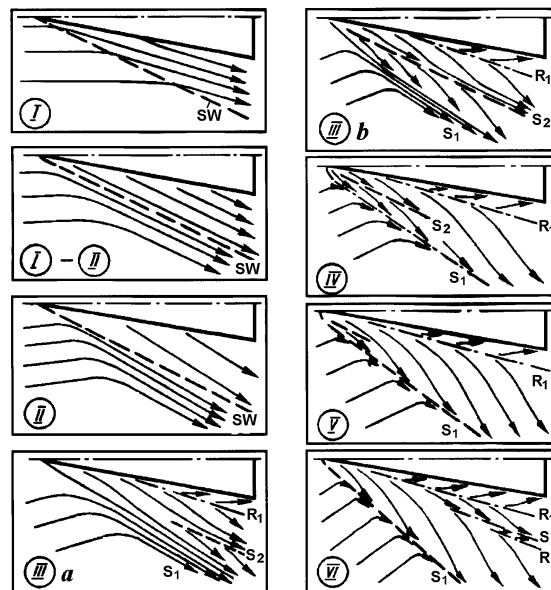


Fig. 52 3-D single fin regimes

and Kim *et al*⁶⁷ is available for Cases 1,3 and 2, respectively. The computations were performed at the same flow conditions as the experiment. The inviscid pressure ratio p_2/p_1 is 2.82, 5.21 and 9.5 for Cases 1 to 3, respectively.

Table 15 Flow Conditions

Case	Reference	Data	M_∞	α	$Re_\delta \times 10^{-5}$
1	Thivet ⁶⁶	RANS	3.0	15°	1.9
	Zheltovodov ^{57, 58}	E	3.0	15°	1.9
2	Thivet ⁶⁶	RANS	4.0	20°	2.1
	Kim <i>et al</i> ⁶⁷	E	4.0	20°	2.1
3	Thivet ⁶⁶	RANS	4.0	30.6°	1.6
	Zheltovodov <i>et al</i> ⁵⁷	E	4.0	30.6°	1.6

Details of the computation are presented in Table 16. Two different turbulence models were examined, namely, the linear Wilcox $k-\omega$ model⁶⁸ (WI) and a weakly nonlinear Wilcox $k-\omega$ model⁶⁹ (WD+). The WD+ model is an extension to compressible flows of the nonlinear correction of Durbin.⁷⁰ In the WD+ model, the coefficient c_μ in the turbulent eddy viscosity $\mu_t = \rho c_\mu k/\omega$ is defined as $c_\mu = \min(c_\mu^0, \sqrt{c_\mu^0}/s)$ where $s = S/\omega$, $S = \sqrt{2S_{ij}S_{ij} - \frac{2}{3}S_{kk}S_{kk}}$ and $S_{ij} = \frac{1}{2}(\partial U_i/\partial x_j + \partial U_j/\partial x_i)$. Computations were performed using the GASPex code.⁷¹ Inviscid fluxes are computed to third order using the Roe scheme with MUSCL reconstruction and a min-mod limiter. Viscous and heat transfer terms are computed using second order central differences. A typical grid is shown in Fig. 53.

The surface streamlines are displayed in Figs. 54 (WI), 55 (experiment) and 56 (WD+) for Case 1, and in Figs. 57 (WI), 58 (experiment) and 59 (WD+) for

Table 16 Details of Computations

Case	Reference	Type	Grid	SA	TA
1	Thivet ⁶⁶	RANS	128 × 160 × 160	2nd	SS
2	Thivet ⁶⁶	RANS	128 × 160 × 160	2nd	SS
3	Thivet ⁶⁶	RANS	112 × 160 × 160	2nd	SS

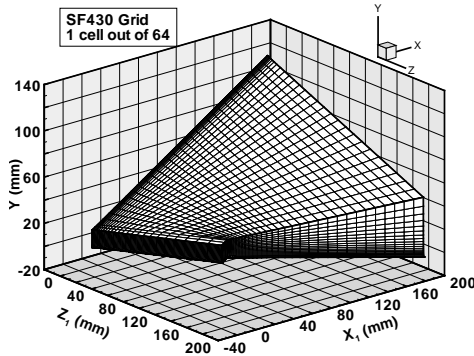


Fig. 53 Grid for 3-D single fin

Case 3. The angle of the primary separation line S_1 is underestimated by the linear (WI) model by 1.4° to 4° , and overestimated by the weakly nonlinear (WD+) model by 1.4° to 2.5° . The angle of the primary attachment line R_1 is accurately predicted by both models. In Case 1 (Regime III), the weak secondary separation S_2 observed in the experiment (Fig. 55) is absent in the computations with WI model (Fig. 54). For the WD+ model (Fig. 56), the distinct changes in the curvature of surface streamlines occurring midway between the fin and primary separation line are similar to incipient secondary separation conditions which occurred in the experiment at a lower fin angle. In Case 3 (Regime VI), the strong secondary separation S_2 and attachment R_2 lines observed in the experiment (Fig. 58) are evident in the WD+ model (Fig. 59) but are entirely absent in the WI model (Fig. 57). This is a significant achievement of the WD+ model.

The computed and experimental pressure distributions are displayed in Figs. 60 to 62. The WD+ model shows a significant improvement compared to the WI model, and, in particular, accurately predicts the appearance of the secondary shock wave associated with the secondary separation.

The computed and experimental skin friction coefficient for Case 2 is shown in Fig. 63. The peak skin friction for the WD+ model is reduced by 35% compared to the WI model. Two series of measurements are shown, where the solid symbols • correspond to corrected values of the skin friction.⁷² The WD+ model displays significantly better agreement with experiment than the WI model.

The improvement achieved by the WD+ model is

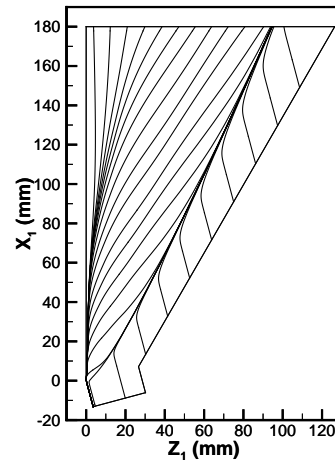


Fig. 54 Surface streamlines for Case 1 (WI)

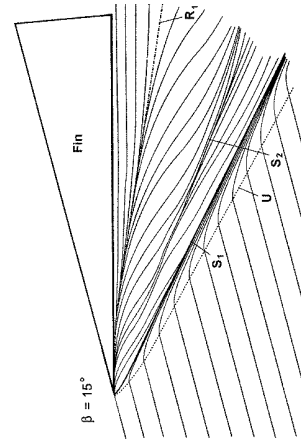


Fig. 55 Surface streamlines for Case 1 (exper)

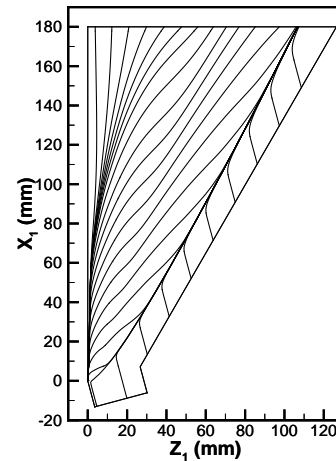


Fig. 56 Surface streamlines for Case 1 (WD+)

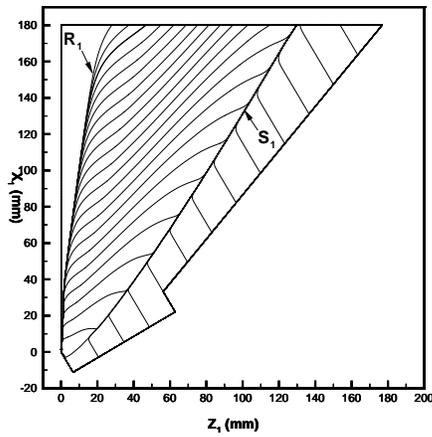


Fig. 57 Surface streamlines for Case 3 (WI)

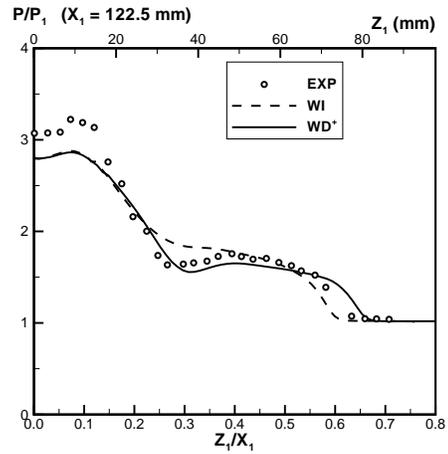


Fig. 60 Surface pressure for Case 1

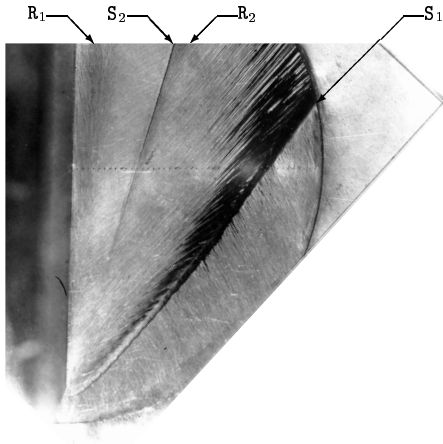


Fig. 58 Surface streamlines for Case 3 (exper)

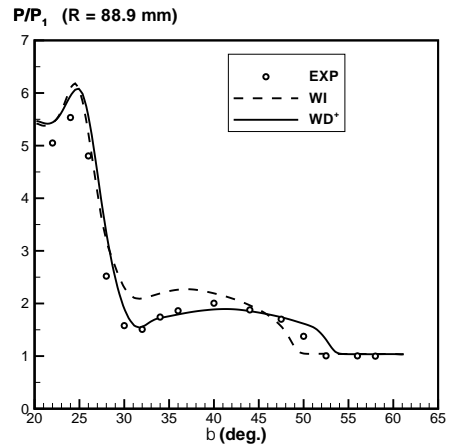


Fig. 61 Surface pressure for Case 2

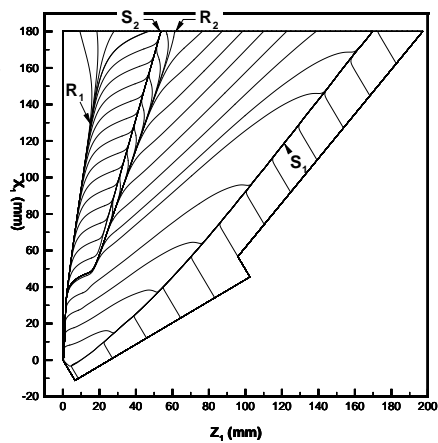


Fig. 59 Surface streamlines for Case 3 (WD+)

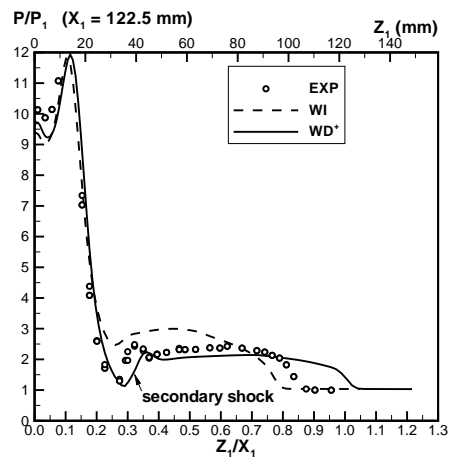


Fig. 62 Surface pressure for Case 3

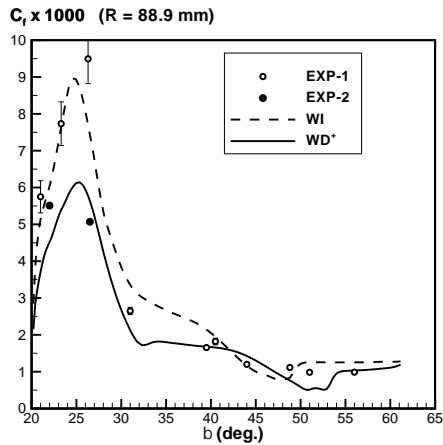


Fig. 63 Skin friction for Case 2

associated with a significant reduction in the peak k within the primary separation vortex core and in the near wall flow penetrating to the place of formation of the secondary separation line. Figs. 64 and 65 display computed turbulence kinetic energy contours for the WI and WD+ models, respectively. The WD+ model reduces the peak k within the core by more than a factor of two, thereby increasing the size of the interaction. These results also support the conclusion of Zheltovodov *et al*^{57, 58, 60} that the turbulence amplification in the reversed flow may be by the reason for the disappearance of the secondary separation in the regime IV - V (Fig. 52).

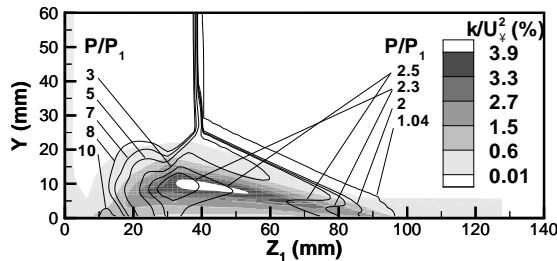


Fig. 64 Turbulence kinetic energy for Case 3 (WI)

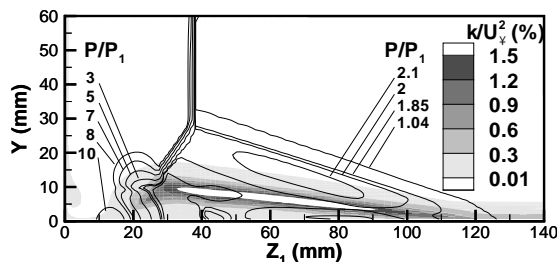


Fig. 65 Turbulence kinetic energy for Case 3 (WD+)

In summary, the following conclusions can be made:

- The weakly nonlinear Wilcox-Durbin (WD+) model provides a significant improvement in prediction of the 3-D single fin interaction in comparison with the Wilcox (WI) model. In particular,
 - The secondary separation/attachment and secondary shock are captured for the Mach 4, $\alpha = 30.6^\circ$ configuration (Regime VI). The linear Wilcox model does not predict secondary separation/attachment and the secondary shock for this case.
 - The surface pressure distribution is in close agreement with experiment for all three cases, except for the position of upstream influence (*i.e.*, the location of initial pressure rise) for the strongest interaction
- The improvement in prediction by the Wilcox-Durbin model is associated with a reduction in the computed turbulence kinetic energy k in the vortex core

3-D Double Fin

The 3-D double fin (crossing shock wave) (Fig. 66) has become a canonical validation case for CFD modeling of shock wave turbulent boundary layer interactions. An equilibrium supersonic turbulent boundary layer approaches a channel defined by two semi-infinite fins of angles α_1 and α_2 separated by a distance W_e at the entrance. Additional geometric parameters include the minimum (throat) width W_t and the offset (if any) of the midpoint of the throat relative to the midpoint of the entrance. The flowfield structure of the double fin interaction has been investigated by several researchers⁷³⁻⁹¹ and the basic topological features have been accurately predicted for weak and moderate interactions; however, a complete understanding of the flow has not yet been achieved. An example of the mean streamline structure is shown in Fig. 67 from Thivet *et al*⁶⁹ for a Mach 4, $7^\circ \times 11^\circ$ double fin interaction. The principal features include the separated boundary layer, vortex, and entrained flow. The computed surface heat transfer coefficient contours and surface streamlines are shown in Fig. 68 and the corresponding experimental surface streamline pattern in Fig. 69. The primary separation lines (denoted S_1 and S_2 in Fig. 69) are evident in both computation and experiment, and correspond to the liftoff of the streamlines from the surface in Fig. 67. The attachment lines (denoted R_1 and R_2 in Fig. 69) correspond to the impingement of the streamlines which demarcate the boundaries of the counter-rotating vortex pair formed by the separated flow. Secondary separation lines (S_3 and S_4 in Fig. 69) and attachment line (denoted R_3 in Fig. 69) are also evident.

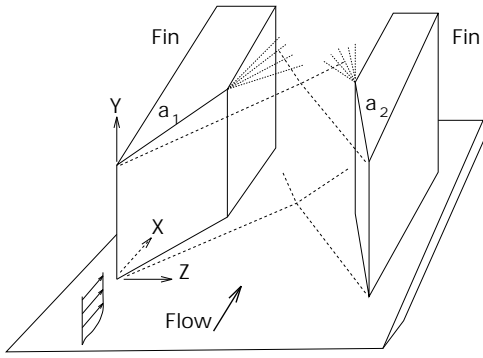


Fig. 66 3-D double fin

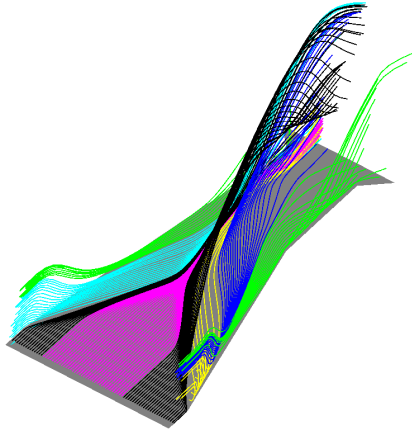


Fig. 67 3-D double fin flow structure

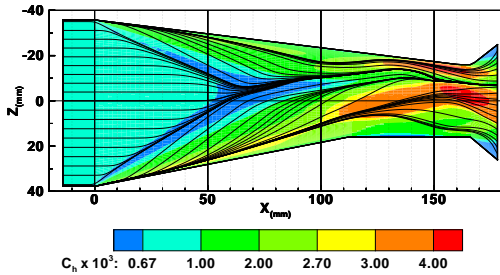


Fig. 68 Computed surface heat transfer

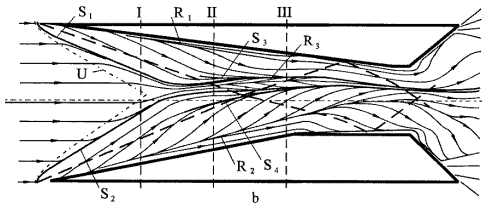


Fig. 69 Surface flow visualization

Cases 1-2: Mach 4, $\alpha_1 = 7^\circ$, $\alpha_2 = 11^\circ$ and Mach 4, $\alpha_1 = 15^\circ$, $\alpha_2 = 15^\circ$

Thivet⁶⁹ simulated two configurations of the 3-D double fin^{xi}. Experimental data of Zheltovodov *et al*

^{xi}A third configuration ($M_\infty = 4$, $\alpha_1 = 7^\circ$, $\alpha_2 = 7^\circ$) is not presented here, as it is a weaker interaction. It is accurately

al^{77-80} is available for both cases. The flow conditions are listed in Table 17. The computations were performed at the same flow conditions as the experiment. The experimental configuration for Case 1 is shown in Fig. 70.

Table 17 Flow Conditions

Case	Reference	Data	M_∞	α_1	α_2	Re_δ $\times 10^{-5}$
1	Thivet ⁶⁹	RANS	3.92	7°	11°	3.0
	Zheltovodov <i>et al</i> ⁷⁷⁻⁸⁰	E	3.92	7°	11°	3.0
2	Thivet ⁶⁹	RANS	3.92	15°	15°	3.0
	Zheltovodov <i>et al</i> ⁷⁷⁻⁸⁰	E	3.92	15°	15°	3.0

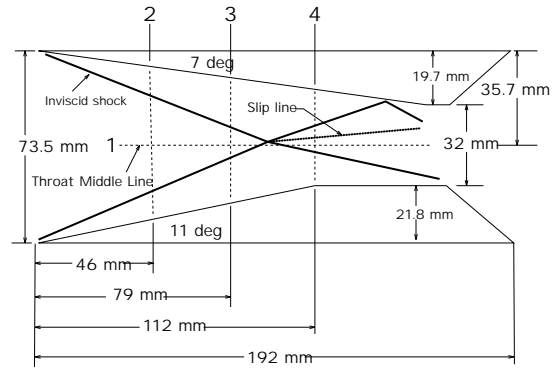


Fig. 70 3-D double fin configuration

Details of the computations^{xii} are presented in Table 18. Five different turbulence models were considered, namely, the (linear) Wilcox $k-\omega$ (WI) model,⁶⁸ and four variants of the Wilcox model based on the requirement for weak realizability⁹² of the computed Reynolds stresses^{xiii}. The variants are the Wilcox-Moore (WM), Wilcox-Durbin (WD) and two modifications thereof (WM+ and WD+). Details of the models are presented in Thivet *et al*.⁶⁹ A detailed grid refinement study⁶⁹ was performed to quantify the uncertainty in the computations.

Table 18 Details of Computations

Case	Reference	Type	Grid	SA	TA
1	Thivet ⁶⁹	RANS	$96 \times 80 \times 160$	2nd	SS
2	Thivet ⁶⁹	RANS	$192 \times 200 \times 104$	2nd	SS

The computed and experimental surface pressure and heat transfer coefficient^{xiv} on the Throat Middle Line (TML)^{xv} for Case 1 are shown in Fig. 71. The

predicted by general RANS models.

^{xii}Data are shown for the finest grid.

^{xiii}Realizability implies that the normal kinematic Reynolds stresses $u'u'$, $v'v'$ and $w'w'$ are non-negative, and the Reynolds shear stresses $u'v'$, $u'w'$ and $v'w'$ are bounded by the Schwartz inequality, e.g., $(u'v')^2 \leq u'u' v'v'$.

^{xiv}The heat transfer coefficient $c_h = q_w / \rho_\infty U_\infty c_p (T_w - T_{aw})$ where T_{aw} is the adiabatic wall temperature.

^{xv}The Throat Middle Line is the streamwise datum through the center of the throat.

surface pressure is accurately predicted by all models with only slight differences in the plateau pressure at $x = 80 - 100$ mm. Similar good agreement with experiment and insensitivity of the predictions to the turbulence model are observed in the spanwise pressure distributions at three streamwise locations (Fig. 72). This is consistent with previous results¹ which showed a marked insensitivity of the computed surface pressure to the turbulence model employed.

The computed surface heat transfer coefficient c_h on the TML (Fig. 71) and at three streamwise locations (Fig. 73) significantly overpredicts the peak experimental value for all models. This is similar to previous results using other RANS models which did not incorporate a specific realizability effect.¹

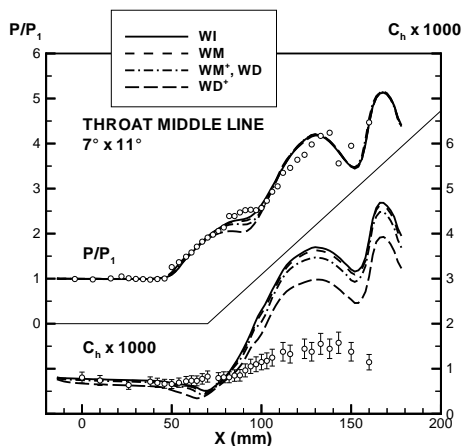


Fig. 71 Surface pressure and heat transfer ($\alpha_1 = 7^\circ, \alpha_2 = 11^\circ$)

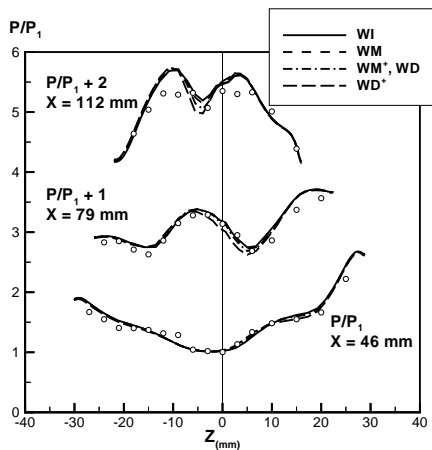


Fig. 72 Surface pressure ($\alpha_1 = 7^\circ, \alpha_2 = 11^\circ$)

The computed and experimental surface pressure and heat transfer coefficient on the Throat Middle Line (TML) for Case 2 are shown in Fig. 74 for the WI and WM+ models. All three models underestimate the location of the pressure rise immediately following the plateau and overestimate the peak pressure. The subsequent expansion (associated with the corner of the

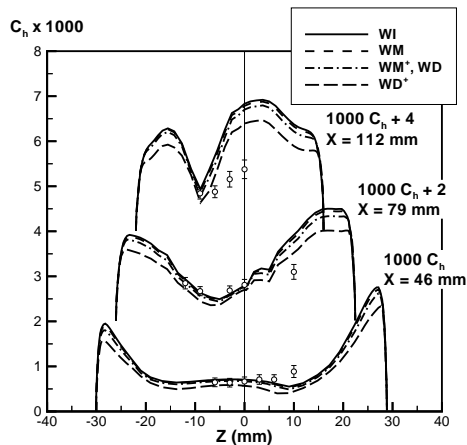


Fig. 73 Surface pressure ($\alpha_1 = 7^\circ, \alpha_2 = 11^\circ$)

fin) is more accurately predicted by the WI model. The computed peak heat transfer significantly overestimates the experiment for all models.

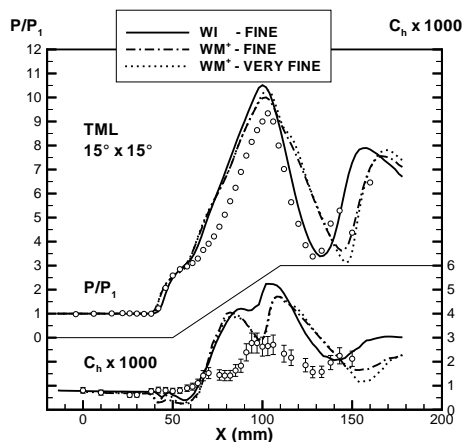


Fig. 74 Surface pressure and heat transfer ($\alpha_1 = 15^\circ, \alpha_2 = 15^\circ$)

Thivet examined the effect of imposing the turbulence length scale limitation proposed by Coakley and Huang.⁹³ The turbulent eddy viscosity $\mu_t = \rho c_\mu k^{1/2} \ell$ and the turbulence length scale ℓ is defined by

$$\ell = \min \left[\ell_{\log}, k^{1/2} / \omega \right]$$

where

$$\ell_{\log} = \frac{\kappa}{c_\mu^{3/4} d}$$

where $\kappa = 0.41$ is von Karman's constant and d is the distance normal to the wall. The dissipation term in the transport equation for k is modeled using $\omega = k^{1/2} \ell$. Fig. 75 displays the ratio of the computed turbulence length scale ℓ (without the Coakley and Huang correction) to the logarithmic expression ℓ_{\log} for Case 1 at $x = 46$ mm for six spanwise locations. The transverse location z_r is zero at the fin and unity

at the location corresponding to the inviscid shock generated by the 11° fin. It is evident that the ratio does not significantly exceed unity, thereby implying that the Coakley and Huang correction would have little effect on the computed solution.

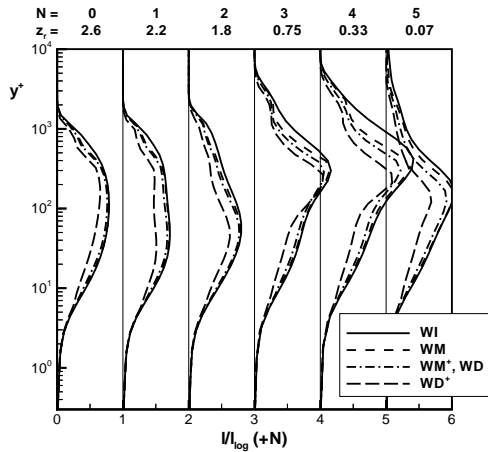


Fig. 75 Turbulence length scale ratio ($\alpha_1 = 7^\circ, \alpha_2 = 11^\circ$)

Thivet also examined the effect of incorporating a compressibility correction⁶⁸ in the $k-\omega$ model^{xvi}. The threshold value of the turbulence Mach number $M_t = \sqrt{2k/a}$ (where a is the local speed of sound) is 0.25 for the compressibility correction. Below this value, the correction is inoperative. The maximum value of M_t using the WI model is 0.3 yielding an increase of only 4% in the dissipation term, thereby implying that this correction (if implemented) would have negligible effect on the computation using the WI model. The values of M_t for the WD, WD+ and WM+ models are everywhere below the threshold, and therefore the compressibility correction (if implemented) would have no effect on these results.

In summary, the following conclusions can be made:

- The computed surface pressure is accurately predicted by the five different turbulence models for Case 1 ($\alpha_1 = 7^\circ, \alpha_2 = 11^\circ$). Some discrepancies between computed and experimental surface pressure are evident for Case 2 ($\alpha_1 = 15^\circ, \alpha_2 = 15^\circ$).
- The peak heat transfer is not accurately predicted by any of the models for either case.
- The proposed length scale correction of Coakley and Huang,⁹³ and the compressibility modifications of Zeman⁹⁴ or Sarkar,⁹⁵ would not significantly change the computed flowfields.

^{xvi}The compressibility correction concept, introduced by Zeman⁹⁴ and Sarkar⁹⁵ to account for the observed decrease in the spreading rate of compressible mixing layers, leads to an undesirable reduction in skin friction for turbulent boundary layers.^{68, 93, 96}

Case 3: Mach 5, $\alpha_1 = \alpha_2 = 18^\circ$

Schmisser and Gaitonde⁹⁷ and Panaras⁹⁸ simulated a Mach 5, $\alpha_1 = \alpha_2 = 18^\circ$ double fin at $Re_\delta = 1.4 \times 10^5$ and isothermal wall conditions ($T_w/T_{aw} = 0.76$). Experimental data of Schuelein and Zheltovodov^{99, 100} (an additional description is presented in Zheltovodov and Maksimov¹⁰¹) is available for this case. The flow conditions are shown in Table 19. The computations were performed at the same flow conditions as the experiment. The experimental configuration is shown in Fig. 76.

Table 19 Flow Conditions

Reference	Data	M_∞	α_1	α_2	Re_δ
Schmisser <i>et al</i> ⁹⁷	RANS	4.96	18°	18°	1.39×10^5
Panaras ⁹⁸	RANS	4.96	18°	18°	1.39×10^5
Schülein and Zheltovodov ⁹⁹⁻¹⁰¹	E	4.96	18°	18°	1.39×10^5

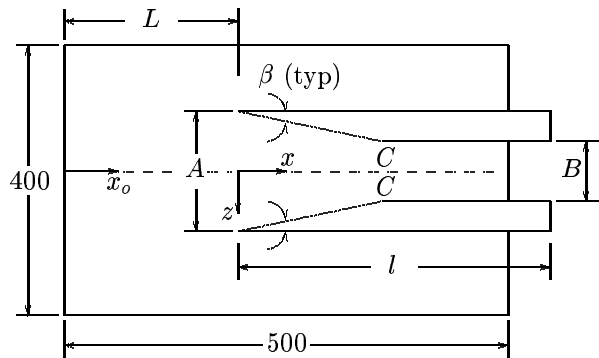


Fig. 76 Double fin configuration

Details of the computations are presented in Table 20. Schmisser and Gaitonde utilized the $k-\epsilon$ model^{102, 103} with low Reynolds number and compressibility corrections. Panaras employed a modified Baldwin-Lomax model.²

Table 20 Details of Computations

Reference	Type	Grid	SA	TA
Schmisser <i>et al</i> ⁹⁷	RANS	$153 \times 143 \times 103$	2nd	ss
Panaras ⁹⁸	RANS	$127 \times 101 \times 91$	2nd	ss

The experimental surface oil flow is presented in Fig. 77, and the computed surface streamlines in Fig. 78 (Schmisser and Gaitonde) and Fig. 79 (Panas). The experiment displays a complex structure of separation (S) and attachment (R) lines. The initial separation lines (S_1 and S_2) generated by the individual fin shock boundary layer interactions coalesce to form a node at the centerline. Corresponding attachment lines (R_1 and R_2) are located near the fins. Additional separation (S_3 to S_6) and attachment lines (R_3 to R_6) form downstream. The central point (S_0^1) is a saddle point in the experiment. In the same region, the computation of Schmisser and Gaitonde

(Fig. 78) displays a node (N_1), while the computation of Panaras (Fig. 79) appears in closer agreement with experiment. Nonetheless, both computed surface streamline plots show overall good agreement with experiment.

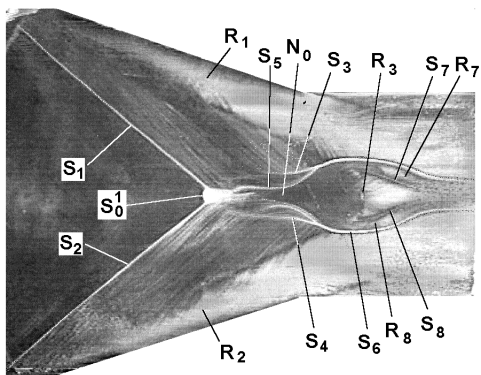


Fig. 77 Experimental surface oil visualization

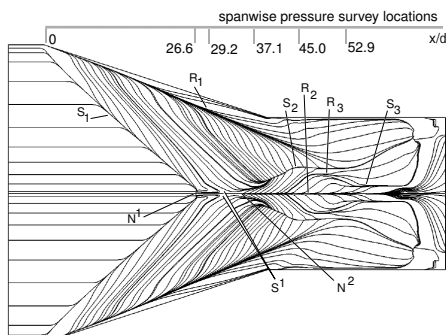


Fig. 78 Surface streamlines

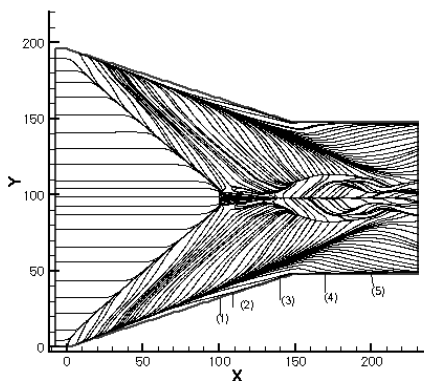


Fig. 79 Surface streamlines

The computed and experimental surface pressure on the centerline is displayed in Fig. 80 (Schmisser and Gaitonde) and Fig. 81 (Panas). The experimental pressure profile displays a rise due to the crossing shock interaction, and a subsequent drop beginning at $x = 42\delta$ due to the expansion originating from the corners C in Fig. 76. The subsequent pressure rise is associated with the reflection of the shocks from the fin surfaces. The computed surface pressure of

Schmisser and Gaitonde shows significant deviation from experiment beginning at the initial plateau in surface pressure. The computed surface pressure of Panaras shows good agreement up to the beginning of the decrease in pressure at $x/\delta = 42$. However, a significant discrepancy appears thereafter.

The computed and experimental surface pressure at three streamwise locations are shown in Figs. 82 to 87. The results of Schmisser and Gaitonde are presented in Figs. 82, 84 and 86, and the results of Panaras in Figs. 83, 85 and 87. Both computations show good agreement with experiment at $x = 26.6\delta$ (Figs. 82 and 83). This location is upstream of the interaction of the crossing shocks, and thus represents individual single fin interactions. At $x = 37.1\delta$ (located at approximately the second focal point N^2 as indicated in Fig. 78) both computed profiles show good agreement with experiment, except for an overshoot in centerline pressure in Fig. 84 (Schmisser and Gaitonde). At $x = 52.9\delta$ (see Fig. 78), both computations show generally good agreement with experiment except for an overshoot in pressure at the centerline.

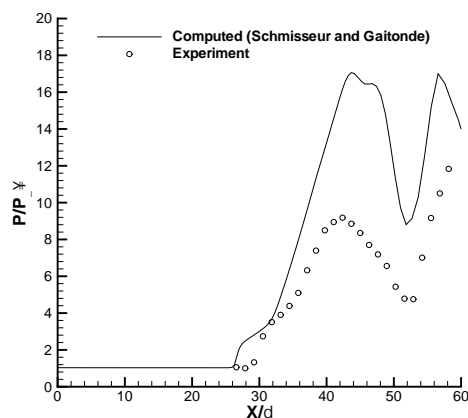


Fig. 80 Surface pressure on centerline

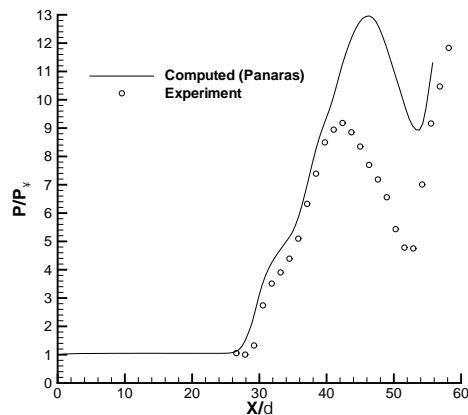


Fig. 81 Surface pressure on centerline

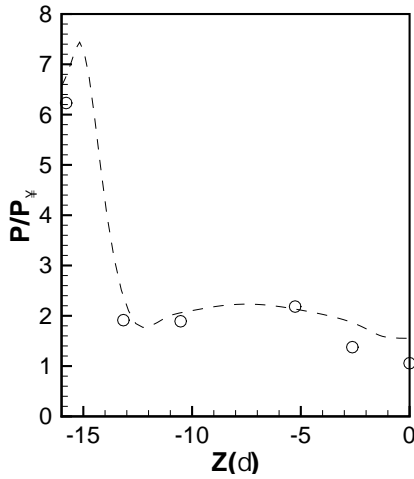


Fig. 82 Surface pressure at $x = 26.6\delta$

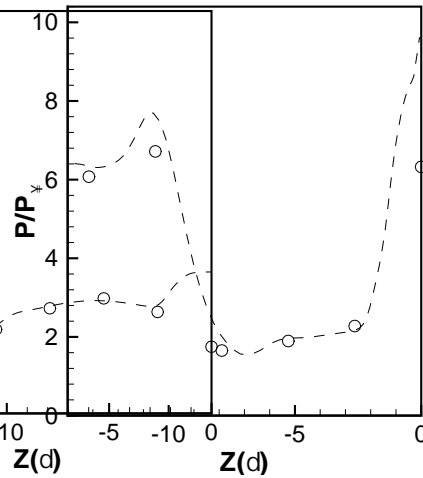


Fig. 84 Surface pressure at $x = 37.1\delta$

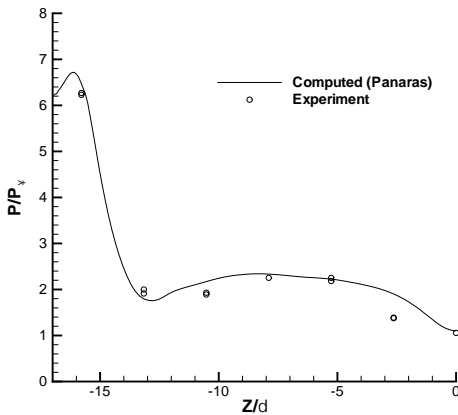


Fig. 83 Surface pressure at $x = 26.6\delta$

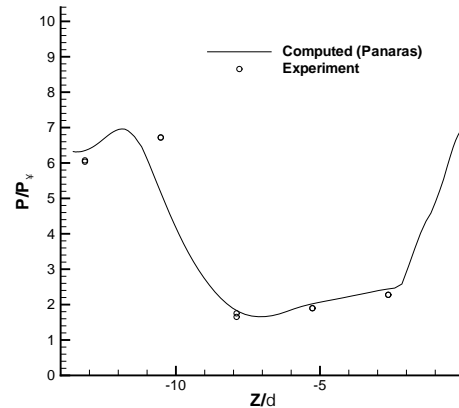


Fig. 85 Surface pressure at $x = 37.1\delta$

In summary, the following conclusions can be made:

- The computed surface streamlines are in good agreement with experiment. The detailed structure of separation, attachment and foci are generally accurately reproduced in the simulations.
- The computed surface pressure shows general agreement with experiment during the initial portion of the interaction and off centerline throughout the entire interaction. However, significant differences between computed and experimental surface pressure are evident on the centerline of the interaction.

Case 4: Mach 5, $\alpha_1 = \alpha_2 = 23^\circ$

Schmisser and Gaitonde^{82, 86, 88, 97} and Panaras⁹⁸ simulated a Mach 5, $\alpha_1 = \alpha_2 = 23^\circ$ double fin at $Re_\delta = 1.4 \times 10^5$ and isothermal wall conditions ($T_w/T_{aw} = 0.76$). Experimental data of Schülein and Zheltovodov^{99, 100} (an additional description is presented in Zheltovodov and Maksimov¹⁰¹) is available for this case. The flow conditions are shown in Table 21. The computations were performed at the same

flow conditions as the experiment. The experimental configuration is shown in Fig. 88.

Table 21 Flow Conditions

Reference	Data	M_∞	α_1	α_2	Re_δ
Schmisser <i>et al</i> ⁹⁷	RANS	4.96	23°	23°	1.39×10^5
Panaras ⁹⁸	RANS	4.96	23°	23°	1.39×10^5
Schülein and Zheltovodov ⁹⁹⁻¹⁰¹	E	4.96	23°	23°	1.39×10^5

Details of the computations^{xvii} are presented in Table 22. Schmisser and Gaitonde utilized the $k-\epsilon$ model^{102, 103} with low Reynolds number and compressibility corrections. Panaras employed a modified Baldwin-Lomax model.²

The experimental surface oil flow is presented in Fig. 89, and the computed surface streamlines in Figs. 90 (Schmisser and Gaitonde) and 91 (Panaras). Good agreement is observed between the computations

^{xvii} Schmisser and Gaitonde performed a grid refinement study using meshes of $91 \times 72 \times 52$, $181 \times 143 \times 103$ and $229 \times 179 \times 129$ and confirmed that the finest grid solution was grid converged.

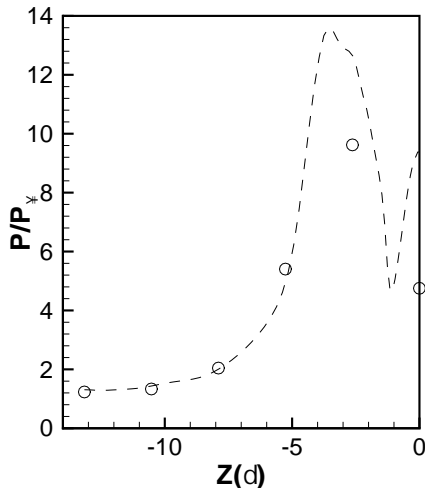


Fig. 86 Surface pressure at $x = 52.9\delta$

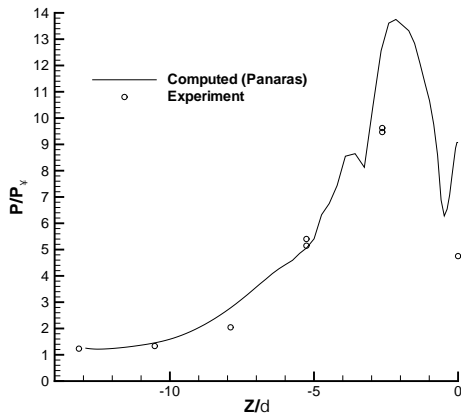


Fig. 87 Surface pressure at $x = 52.9\delta$

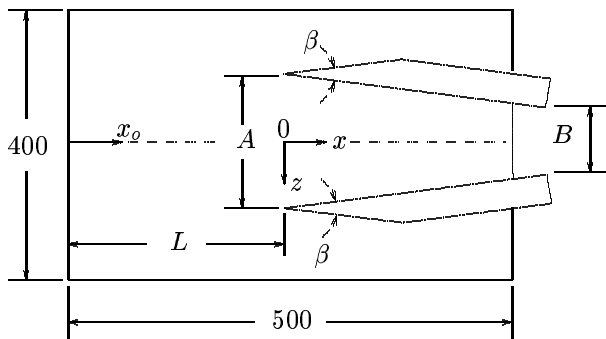


Fig. 88 Double fin configuration

and experiment.

Table 22 Details of Computations

Reference	Type	Grid	SA	TA
Schmisser <i>et al</i> ⁹⁷	RANS	229 × 179 × 129	2nd	SS
Panaras ⁹⁸	RANS	117 × 101 × 91	2nd	SS

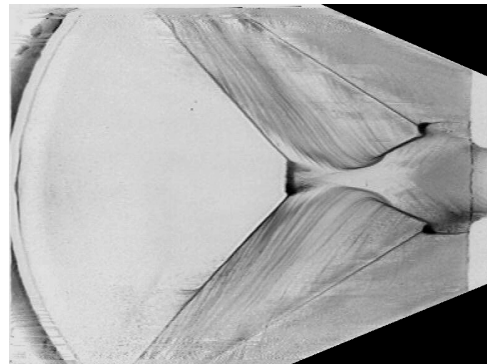


Fig. 89 Experimental surface oil visualization

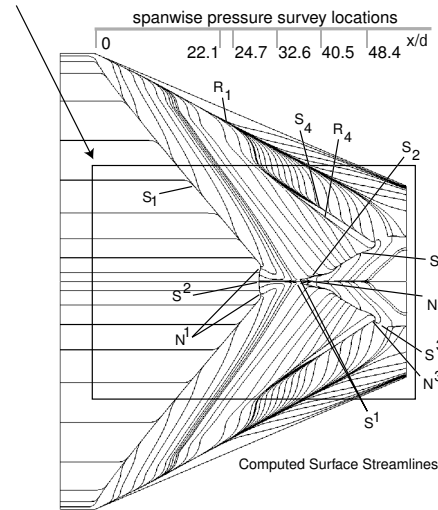


Fig. 90 Surface streamlines

The computed and experimental surface pressure on the centerline is displayed in Fig. 92 (Schmisser and Gaitonde) and Fig. 93 (Panaras). The experimental profile is similar to the $18^\circ \times 18^\circ$ configuration except for the absence of the second shock reflection on the centerline due to the limited length of the flat plate. The computed profile by Schmisser and Gaitonde shows good agreement with experiment up to the peak experiment pressure, but significantly overestimates experiment downstream. The computed profile by Panaras also shows good agreement with experiment up to the peak pressure, but does not display the expansion region^{xviii} observed in the experiment.

The computed and experimental surface pressure

^{xviii}A separate coarse grid computation was performed by Panaras¹⁰⁴ wherein the effect of the finite plate length was approximated by adding a divergent section to the flat plate. The computed centerline pressure displayed significantly better agreement with experiment.

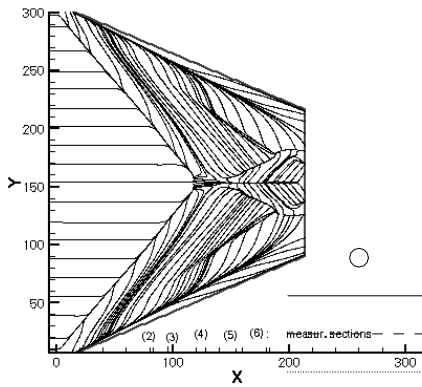


Fig. 91 Surface streamlines

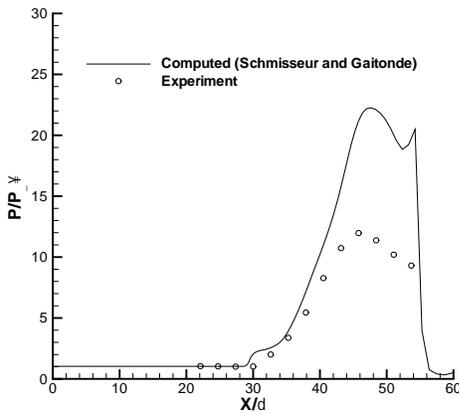


Fig. 92 Surface pressure on centerline

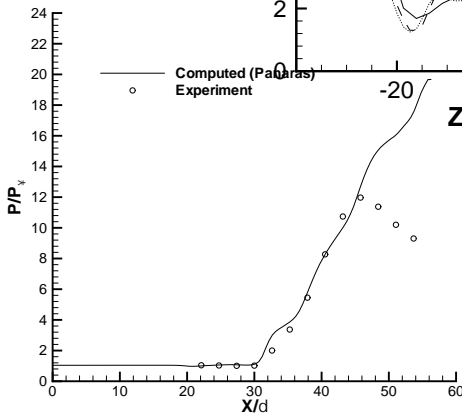


Fig. 93 Surface pressure on centerline

at three streamwise locations are shown in Figs. 94 to 99. The results of Schmisseur and Gaitonde are shown in Figs. 94, 96 and 98, and the results of Panaras in Figs. 95, 97 and 99. Both computations are in close agreement with the available experimental data at $x = 22.1\delta$ which is upstream of the crossing shock interaction (see Figs. 92 and 93). At $x = 32.6\delta$, lo-

cated in the midst of the crossing shock interaction, both computations show close agreement with experiment, although somewhat overestimating the centerline pressure. At $x = 48.4\delta$, the agreement between computation and experiment is good except in the immediate vicinity of the centerline where the pressure is overestimated.

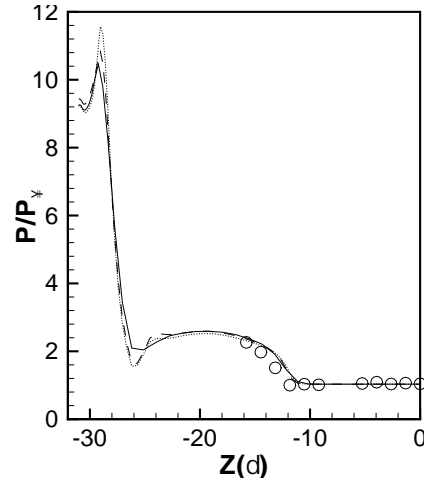


Fig. 94 Surface pressure at $x = 22.1\delta$

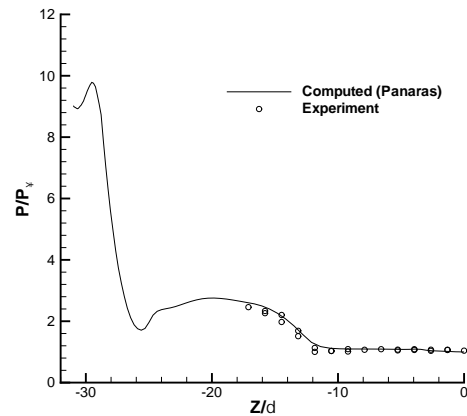


Fig. 95 Surface pressure at $x = 22.1\delta$

In summary, the following conclusions can be made:

- The computed surface streamlines display good agreement with experiment
- The computed surface pressure shows general agreement with experiment during the initial portion of the interaction and off centerline throughout the entire interaction. However, significant differences between computed and experimental surface pressure are evident on the centerline, similar to Case 3.

Conclusions

An evaluation of the CFD capability for prediction of shock wave turbulent boundary layer interaction was performed under the auspices of NATO

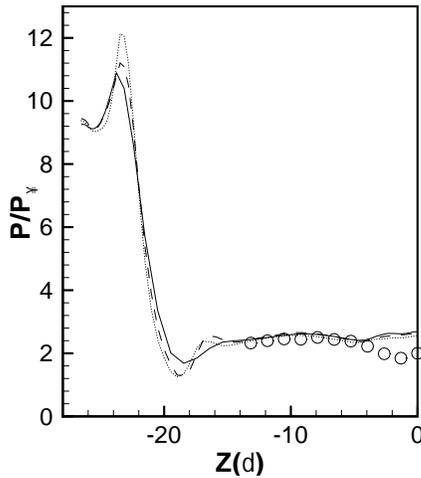


Fig. 96 Surface pressure at $x = 32.6\delta$

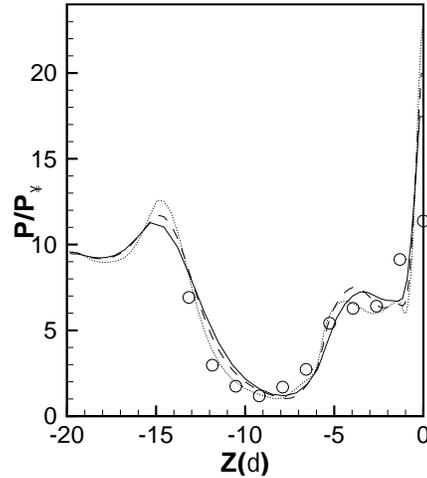


Fig. 98 Surface pressure at $x = 48.4\delta$

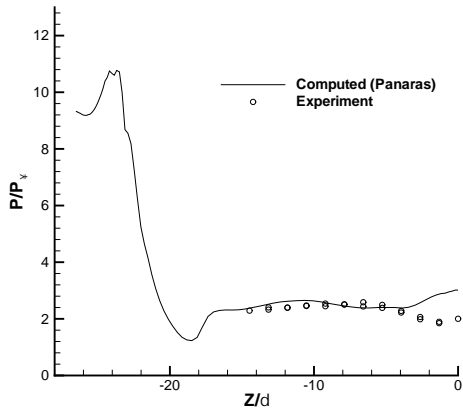


Fig. 97 Surface pressure at $x = 32.6\delta$

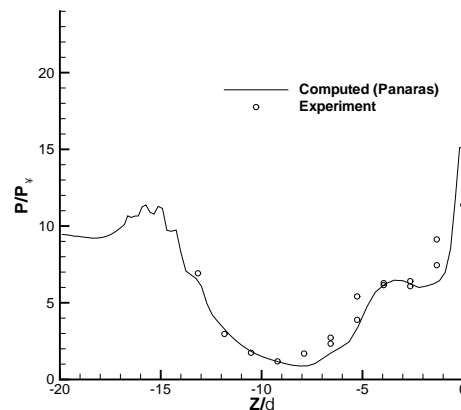


Fig. 99 Surface pressure at $x = 48.4\delta$

RTO Working Group 10. Five separate configurations were considered, namely, the 2-D compression corner, 2-D expansion-compression corner, 2-D shock impingement, 3-D single fin and 3-D double fin. Recent DNS, LES and RANS simulations were solicited. The computed results were compared with experimental data where available. The following conclusions may be drawn:

- DNS and LES
 - DNS and LES of shock wave turbulent boundary layer interaction is an active area of research. In the previous review of shock wave turbulent boundary layer interaction by Knight and Degrez¹ published in 1998, there were no DNS or LES results available. The present paper includes several DNS and LES results for 2-D shock wave turbulent boundary layer interactions.
 - A comprehensive assessment of the capability of DNS and LES was not possible for two reasons. First, the DNS and LES simulations

have been performed at lower Reynolds numbers Re_δ than the experiment for all cases except one (*i.e.*, the 2-D shock impingement). Second, the DNS and LES have been performed for nominally 2-D flows. Both reasons are attributable to the computational cost of DNS and LES.

- Although the set of comparisons between DNS and LES with experiment was limited, nevertheless it is clear that significant progress has been achieved in the prediction of shock wave turbulent boundary layer interaction using DNS and LES. In several cases, the computations were performed at Reynolds numbers close to the experiment (and, in one case, equal to experiment), and good agreement with experimental data was achieved. Detailed comparisons included surface pressure, skin friction, velocity, temperature and turbulence profiles. However, some significant discrepancies are evident, due possibly to the differences in Reynolds

number.

- No DNS or LES results for surface heat transfer in shock wave turbulent boundary layer interaction were available. This is particularly disappointing, since prior RANS simulations of strongly separated shock wave turbulent boundary layer interactions have failed to accurately predict heat transfer.¹
- RANS
 - New ideas in modeling have reinvigorated RANS simulations for shock wave turbulent boundary layer interaction. These new ideas include realizability (weak nonlinearity) and specific physical models which incorporate known flowfield behavior.
 - The weakly nonlinear Wilcox-Durbin model successfully predicts secondary separation for the 3-D single fin in agreement with experiment.
 - The linear and weakly nonlinear Wilcox-based models fail to accurately predict surface heat transfer for the separated 3-D double fin.
 - The surface streamline pattern for the 3-D double fin Case Nos. 3 and 4 is predicted by both the conventional $k-\epsilon$ and Baldwin-Lomax-Panaras models.
 - The surface pressure for the 3-D double fin is accurately predicted by the conventional $k-\epsilon$ and Baldwin-Lomax-Panaras models only in the initial region of the interaction. Significant differences between the computational and experimental centerline pressure are evident downstream.

Future Needs

The following research needs for shock wave turbulent boundary layer interaction may be identified:

- DNS and LES simulations are needed at Reynolds numbers corresponding to the experiment. This is essential to end speculation regarding the reasons for discrepancy between simulation and experiment.
- DNS and LES simulations are needed for 3-D configurations. All DNS and LES results to date have been for nominally 2-D flows.
- DNS and LES simulations are needed to compare with experimental data for heat transfer. Neither DNS, LES nor RANS models to date have successfully predicted surface heat transfer in strongly separated shock wave turbulent boundary layer interactions.

- RANS modeling needs continued emphasis on weakly nonlinear corrections to two equation models, and continued development of configuration-specific modifications to simple models.

Acknowledgments

This research is supported by AFOSR under Grant No. F49620-99-1-0008 monitored by Drs. Robert Herklotz, L. Sakell, J. Schmisser and Steve Walker, by the SCOPES 2000-2003 Program under Project No. 7SUPJ062351 and by the Russian Foundation of Basic Research under Grant No. 97-01-00885.

References

- ¹Knight, D., and Degrez, G., "Shock Wave Boundary Layer Interactions in High Mach Number Flows – A Critical Survey of Current CFD Prediction Capabilities", AGARD AR-319, Volume 2, 1998.
- ²Panaras, A., "The Effect of the Structure of Swept Shock Wave Turbulent Boundary Layer Interactions on Turbulence Modeling", *Journal of Fluid Mechanics*, Vol. 338, 1997, pp. 203–230.
- ³Zhel'tovodov, A., "Shock Waves / Turbulent Boundary Layer Interactions - Fundamental Studies and Applications", AIAA Paper 96-1977, 1996.
- ⁴Muylaert, J., Ed., "Technologies for Propelled Hypersonic Flight", EWP NR. 2122, European Space Agency, May 2001.
- ⁵Knight, D., "Overview of NATO RTO WG 10 SG 3: CFD Validation for Propelled Hypersonic Flight", AIAA Paper No. 2002-0433, Jan 2002.
- ⁶<http://www.engr.rutgers.edu/~wg10>
- ⁷Dolling, D., and Murphy, M., "Wall Pressure Fluctuations in a Supersonic Separation Compression Ramp Flowfield", AIAA Paper No. 82-0986, 1982.
- ⁸Andreopoulos, J., and Muck, K., "Some New Aspects of the Shock Wave Boundary Layer Interaction in Compression-ramp Flows", *Journal of Fluid Mechanics*, Vol. 180, 1987, pp. 405–428.
- ⁹Dolling, D., "Considerations in the Comparison of Experimental Data with Simulations – Consistency of Math Models and Flow Physics", AIAA Paper No. 96-2030, 1996.
- ¹⁰Dolling, D., "Fifty Years of Shock Wave Boundary Layer Interaction – What Next?", AIAA Paper No. 2000-2596, 2000.
- ¹¹Green, J., "Interactions Between Shock Waves and Turbulent Boundary Layers", *Progress in Aerospace Sciences*, Vol. 11, 1970, pp. 235–341.
- ¹²Delery, J., "Shock Wave/Turbulent Boundary Layer Interaction and Its Control", *Progress in Aerospace Sciences*, Vol. 22, 1985, pp. 209–280.
- ¹³Zhel'tovodov, A., Schülein, E., "The Peculiarities of Turbulent Separation Development in Disturbed Boundary Layers", *Modelirovaniye v Mekhanike*, Vol. 2, No. 1, 1988, pp. 53–58 (in Russian).
- ¹⁴Zhel'tovodov, A., Schülein, E., and Horstman, C., "Development of Separation in the Region Where a Shock Interacts with a Turbulent Boundary Layer Perturbed by Rarefaction Waves", *Journal of Applied Mechanics and Technical Physics*, Vol. 34, No. 3, May-June 1993, pp. 346–354.
- ¹⁵Zukoski, E., "Turbulent Boundary Layer Separation in Front of a Forward Facing Step", *AIAA Journal*, Vol. 5, No. 10, 1967, pp. 1746–1753.
- ¹⁶Shang, J. and Hankey, W., Jr., "Numerical Solution for Supersonic Turbulent Flow over a Compression Corner", *AIAA Journal*, Vol. 13, No. 10, pp. 1368–1375, October 1975.

- ¹⁷Horstman, C. and Hung, C., "Reynolds Number Effects on Shock-Wave Turbulent Boundary-Layer Interaction - A Comparison of Numerical and Experimental Results", AIAA Paper 77-42, 1977.
- ¹⁸Visbal, M. and Knight, D., "The Baldwin-Lomax Turbulence Model for Two-Dimensional Shock-Wave/Boundary-Layer Interactions", *AIAA Journal*, Vol. 22, No. 7, pp. 921-928, July 1984.
- ¹⁹Ong, C. and Knight, D., "Hybrid MacCormack and Implicit Beam-Warming Algorithms for a Supersonic Compression Corner", *AIAA Journal*, Vol. 25, No. 3, pp. 401-407, March 1987.
- ²⁰Horstman, C., and Zheltovodov, A. "Numerical Simulation of Shock Waves/Expansion Fans - Turbulent Boundary Layer Interaction", International Conference on Methods of Aerophysical Research, Institute of Theoretical and Applied Mechanics, Russian Academy of Sciences, Novosibirsk, Russia, July 1994, Part 2, pp. 118-125.
- ²¹Borisov, A., Zheltovodov, A., Maksimov, A., Fedorova, N. and Shpak, S., "Verification of Turbulence Models and Computational Methods of Supersonic Separated Flows", *International Conference on Methods of Aerophysical Research*, Institute of Theoretical and Applied Mechanics, Russian Academy of Sciences, Novosibirsk, Russia, July 1996, Part 1, pp. 54-61.
- ²²Urbain, G., Knight, D., and Zheltovodov, A., "Compressible Large Eddy Simulation using Unstructured Grid: Supersonic Turbulent Boundary Layer and Compression Corner", AIAA Paper No. 99-0427, 1999.
- ²³Zheltovodov, A., and Yakovlev, V., "Stages of Development, Flowfield Structure and Turbulence Characteristics of Compressible Separated Flows in the Vicinity of 2-D Obstacles", Preprint No. 27-86, Institute of Theoretical and Applied Mechanics, USSR Academy of Sciences, Novosibirsk, 1986, 56 pp. (in Russian).
- ²⁴Zheltovodov, A., Schülein, E., Yakovlev, V., "Development of Turbulent Boundary Layer under Conditions of Mixed Interaction with Shock and Expansion Waves", Preprint No. 28-83, Institute of Theoretical and Applied Mechanics, USSR Academy of Sciences, Novosibirsk 1983, 51 p. (In Russian).
- ²⁵Zheltovodov, A., Trofimov, V., Schülein, E., and Yakovlev, V., "An Experimental Documentation of Supersonic Turbulent Flows in the Vicinity of Forward- and Backward-Facing Ramps", Report No. 2030, Institute of Theoretical and Applied Mechanics, USSR Academy of Sciences, 1990.
- ²⁶White, F., *Viscous Fluid Flow*, McGraw-Hill, 1974, New York.
- ²⁷Muck, K., Spina, E., and Smits, A., "Compilation of Turbulence Data for an 8 degree Compression Corner at Mach 2.9", Report MAE-1642, Princeton University, Department of Mechanical and Aerospace Engineering, April 1984.
- ²⁸Smits, A., and Dussauge, J.-P., *Turbulent Shear Layers in Supersonic Flow*, American Institute of Physics, Woodbury, NY, 1996.
- ²⁹Adams, N., "Direct Numerical Simulation of Turbulent Supersonic Boundary Layer Flow", *Advances in DNS and LES - First AFOSR International Conference on DNS and LES*, Greydon Press, Columbus, OH, 1997, pp. 29-40.
- ³⁰Adams, N., "Direct Numerical Simulation of Turbulent Compression Ramp Flow", *Theoretical and Computational Fluid Dynamics*, Vol. 12, No. 2, 1998, pp. 109-129.
- ³¹Adams, N., "Direct Simulation of the Turbulent Boundary Layer Along a Compression Ramp at $M = 3$ and $Re_\theta = 1685$ ", *Journal of Fluid Mechanics*, Vol. 420, 2000, pp. 47-83.
- ³²Rizzetta, D., Visbal, M., and Gaitonde, D., "Direct Numerical and Large Eddy Simulation of Supersonic Flows by a High-Order Method", AIAA Paper No. 2000-2408, January 2000.
- ³³Germano, M., Piomelli, U., Moin, P., and Cabot, W., "A Dynamic Subgrid-Scale Eddy Viscosity Model", *Physics of Fluids A*, Vol. 3, No. 7, July 1991, pp. 1760-1765.
- ³⁴VanDriest, E., "Turbulent Boundary Layers in Compressible Fluids", *Journal of the Aeronautical Sciences*, Vol. 18, No. 3, March 1951, pp. 145-160.
- ³⁵Tennekes, H. and Lumley, J., *A First Course in Turbulence*, The MIT Press, 1972, Cambridge, MA.
- ³⁶Rizzetta, D., and Visbal, M., "Large Eddy Simulation of Supersonic Compression Ramp Flows", AIAA Paper No. 2001-2858, June 2001.
- ³⁷Settles, G., Fitzpatrick, T., and Bogdonoff, S., "Detailed Study of Attached and Separated Compression Corner Flowfields in High Reynolds Number Supersonic Flow", *AIAA Journal*, Vol. 17, No. 6, 1979, pp. 579-585.
- ³⁸Dolling, D., and Murphy, M., "Unsteadiness of the Separation Shock Wave Structure in a Supersonic Compression Ramp Flowfield", *AIAA Journal*, Vol. 21, No. 12, 1983, pp. 1628-1634.
- ³⁹Smits, A., and Muck, K., "Experimental Study of Three Shock Wave Turbulent Boundary Layer Interactions", *Journal of Fluid Mechanics*, Vol. 182, Sept 1987, pp. 291-314.
- ⁴⁰Yan, H., Knight, D., and Zheltovodov, A., "Large Eddy Simulation of Supersonic Compression Corner Using ENO Scheme", Third AFOSR International Conference on DNS and LES, Arlington, Texas, August 2001.
- ⁴¹Borisov, A., Zheltovodov, A., Maksimov, A., Fedorova, N., and Shpak, S., "Experimental and Numerical Study of Supersonic Turbulent Separated Flows in the Neighborhood of Two-Dimensional Obstacles", *Fluid Dynamics*, 2000, Vol. 34, No. 2, pp. 181-189 (in English).
- ⁴²J. Boris, F. Grinstein, E. Oran, and R. Kolbe. New Insights into Large Eddy Simulation. *Fluid Dynamics Research*, 10:199-228, 1992.
- ⁴³Knight, D., Yan, H., and Zheltovodov, A., "Large Eddy Simulation of Supersonic Turbulent Flow in Expansion-Compression Corner", *Third AFOSR International Conference on DNS and LES*, Arlington, TX, Aug 2001.
- ⁴⁴Zheltovodov, A. Zaulichniy, E., Trofimov, V., and Yakovlev, V. "The Study of Heat Transfer and Turbulence in Compressible Separated Flows", Preprint No. 22-87, Institute of Theoretical and Applied Mechanics, USSR Academy of Sciences, Novosibirsk, 1987, 48 pp. (in Russian).
- ⁴⁵Zheltovodov, A., Zaulichniy, E., Trofimov, V., "Development of Models for Calculations of Heat Transfer under Conditions of Supersonic Turbulent Separated Flows", *Prikladnaya Mekhanika i Tekhnicheskaya Fizika*, 1990, No. 4, pp. 96-104 (in Russian).
- ⁴⁶Zheltovodov, A., Horstman, C., "Experimental and Numerical Investigation of 2-D Expansion/Shock Wave - Turbulent Boundary Layer Interactions", Preprint No. 2-93, Institute of Theoretical and Applied Mechanics, Russian Academy of Sciences, Novosibirsk, 1993, 25 pp.
- ⁴⁷Zheltovodov, A., Mecler, L., and Schülein, E., "Peculiarities of Development of Separated Flows in Compression Corners After the Expansion Fans", Preprint No. 10-87, Institute of Theoretical and Applied Mechanics, USSR Academy of Sciences, Novosibirsk, 1987, 47 pp. (in Russian).
- ⁴⁸Zheltovodov, A., Trofimov, V., Filippova, E., and Yakovlev, Y., "Influence of Turbulence Change on the Heat Exchange Under the Conditions of Supersonic Separated Flows", in *Abstracts: IUTAM Symposium on Separated Flows and Jets*, USSR Academy of Sciences, Siberian Division, Novosibirsk, 1990, pp. 273-274.
- ⁴⁹Kuehn, D., "Experimental Investigation of the Pressure Rise Required for Incipient Separation of Turbulent Boundary Layers in Two-Dimensional Supersonic Flow", NASA Memo 1-21-59A, NASA/TIL/6209, 1959.
- ⁵⁰Garnier, E., "Simulation des Grandes Échelles en Régime Transsonique", Le Grade de Docteur en Sciences de l'Université Paris XI Orsay, 27 October 2000.
- ⁵¹Garnier, E., "Large Eddy Simulation of Shock Boundary

Layer Interaction”, Third AFOSR International Conference on DNS and LES, Arlington, TX, August 2001.

⁵²Deleuze, J., “Structure d’une couche limite turbulente soumise à une de choc incidente”, Thèse de doctorat, Université Aix-Marseille II, 1995.

⁵³Laurent, H., “Turbulence d’une interaction onde de choc / couche limite sur une paroi adiabatique ou chauffée”, Thèse de Doctorat, Université Aix-Marseille II, 1996.

⁵⁴Sagaut, P., *Large Eddy Simulation for Incompressible Flows*, Springer-Verlag, Berlin, 2001.

⁵⁵Lenormand, E., Sagaut, P., Ta Phuoc, L., and Comte, P., “Subgrid-scale Models for Large-Eddy Simulation of Compressible Wall Bounded Flows”, *AIAA Journal*, Vol. 38, No. 8, 2000, pp. 1340–1350.

⁵⁶Lenormand, E., Sagaut, P., and Ta Phuoc, L., “Large Eddy Simulation of Subsonic and Supersonic Channel Flow at Moderate Reynolds Number”, *International Journal for Numerical Methods in Fluids*, Vol. 32, 2000, pp. 369–406.

⁵⁷Zhel'tovodov, A., “Regimes and Properties of Three-Dimensional Separation Flows Initiated by Skewed Compression Shocks”, *Journal of Applied Mechanics and Technical Physics*, Vol. 23, No. 3, May-June 1982, pp. 413–418.

⁵⁸Zhel'tovodov, A., and Schülein, E., “Three Dimensional Interaction of Swept Shock Waves with Turbulent Boundary Layer in Corner Configurations”, Institute of Theoretical and Applied Mechanics Preprint 34-86, USSR Academy of Sciences, Novosibirsk, 1986, 49 pp. (in Russian).

⁵⁹Settles, G., and Dolling, D., “Swept Shock Wave Boundary Layer Interactions”, in *Tactical Missile Aerodynamics*, AIAA Progress in Astronautics and Aeronautics (J. Nielsen, Ed.), 1986, pp. 297–379.

⁶⁰Zhel'tovodov, A., Maksimov, A., Schülein, E., “Development of Turbulent Separated Flows in the Vicinity of Swept Shock Waves”, in *The Interactions of Complex 3-D Flows* (A. Kharitonov, Ed.), Institute of Theoretical and Applied Mechanics, Siberian Branch of the USSR Academy of Sciences, Novosibirsk, 1987, pp. 67–91.

⁶¹Knight, D., Horstman, C., Settles, G., and Zhel'tovodov, A., “Three-Dimensional Shock Wave Turbulent Boundary Layer Interactions Generated by a Single Fin”, *Thermophysics and Aeromechanics*, Vol. 5, No. 2, 1998, pp. 131–140.

⁶²Settles, G., and Dolling, D., “Swept Shock Boundary Layer Interactions - Tutorial and Update”, AIAA Paper No. 90-0375, 1990.

⁶³Alvi, F., and Settles, G., “A Physical Model of the Swept Shock Boundary Layer Interaction Flowfield”, AIAA Paper No. 91-1768, 1991.

⁶⁴Knight, D., Badekas, D., Horstman, C., and Settles, G., “Quasiconical Flowfield Structure of the Three Dimensional Single Fin Interactino”, *AIAA Journal*, Vol. 30, No. 12, Dec 1992, pp. 2809–2816.

⁶⁵Panaras, A., “Review of the Physics of Swept Shock Boundary Layer Interactions”, *Progress in Aerospace Sciences*, Vol. 32, 1996, pp. 173–244.

⁶⁶Thivet, F., Knight, D., Zhel'tovodov, A., and Maksimov, A., “Importance of Limiting the Turbulence Stresses to Predict 3D Shock Wave Boundary Layer Interactions”, *23rd International Symposium on Shock Waves*, Ft. Worth, TX, July 2001.

⁶⁷Kim, K., Lee, Y., Alvi, F., Settles, G., and Horstman, C., “Skin Friction Measurements and Computational Comparison of Swept Shock Boundary Layer Interactions”, *AIAA Journal*, Vol. 29, No. 10, 1991, pp 1643–1650.

⁶⁸Wilcox, D., *Turbulence Modeling for CFD*, DCW Industries, Inc., La Cañada, CA, 1993.

⁶⁹Thivet, F., Knight, D., Zhel'tovodov, A., and Maksimov, A., “Insights in Turbulence Modeling for Crossing Shock Wave Turbulent Boundary Layer Interactions”, *AIAA Journal*, Vol. 39, No. 6, June 2001, pp. 985–995.

⁷⁰Durbin, P., “On the $k-\epsilon$ Stagnation Point Anomaly”, *International Journal of Heat and Fluid Flow*, Vol. 17, No. 1, 1996, pp. 89–90.

⁷¹Aerosoft, Inc., *General Aerodynamic Simulation Program Version 3 User's Manual*, Aerosoft, Inc., Blacksburg, VA, 1996.

⁷²Settles, G., Private Communication.

⁷³Garrison, T., Settles, G., Narayanswami, N., and Knight, D., “Structure of Crossing Shock Wave Turbulent Boundary Layer Interactions”, *AIAA Journal*, Vol. 31, No. 12, 1993, pp. 2204–2211.

⁷⁴Garrison, T., Settles, G., Narayanswami, N., and Knight, D., “Laser Interferometer Skin Friction Measurements of Crossing Shock Wave Turbulent Boundary Layer Interactions”, *AIAA Journal*, Vol. 32, No. 6, 1994, pp. 1234–1241.

⁷⁵Gaitonde, D., Shang, J., and Visbal, M., “Structure of a Double Fin Turbulent Interaction at High Speed”, *AIAA Journal*, Vol. 33, No. 2, 1995, pp. 193–200.

⁷⁶Gaitonde, D., and Shang, J., “Structure of a Double Fin Turbulent Interaction at Mach 4”, *AIAA Journal*, Vol. 33, No. 12, 1995, pp. 2250–2258.

⁷⁷Zhel'tovodov, A., Maksimov, A., Shevchenko, A., Vorontsov, S., and Knight, D., “Experimental Study and Computational Comparison of Crossing Shock Wave Turbulent Boundary Layer Interactions”, *International Conference on Methods of Aerophysical Research*, Institute of Theoretical and Applied Mechanics, Siberian Branch of Russian Academy of Sciences, Novosibirsk, 1994, pp. 221–230.

⁷⁸Zhel'tovodov, A., Maksimov, A., and Shevchenko, A., “Topology of Three Dimensional Separation Under the Conditions of Symmetric Interaction of Crossing Shocks and Expansion Waves with Turbulent Boundary Layer”, *Thermophysics and Aeromechanics*, Vol. 5, No. 3, 1998, pp. 293–312.

⁷⁹Zhel'tovodov, A., Maksimov, A., Shevchenko, A., and Knight, D., “Topology of Three Dimensional Separation Under the Conditions of Asymmetric Interaction of Crossing Shocks and Expansion Waves with Turbulent Boundary Layer”, *Thermophysics and Aeromechanics*, Vol. 5, No. 4, 1998, pp. 483–503.

⁸⁰Zhel'tovodov, A., Maksimov, A., “Symmetric and Asymmetric Crossing-Shock-Waves/Turbulent Boundary Layer Interactions”, Final Technical Report, EOARD Contract F61708-97-W0136, Institute of Theoretical and Applied Mechanics, Siberian Branch of Russian Academy of Sciences, Novosibirsk, 1998, 76 pp.

⁸¹Gaitonde, D., Visbal, M., Shang, J., Zhel'tovodov, A., and Maksimov, A., “Sidewall Interaction in an Asymmetric Simulated Scramjet Inlet Configuration”, *Journal of Propulsion and Power*, Vol. 17, No. 3, 2001, pp. 579–584.

⁸²Zhel'tovodov, A., Maksimov, A., Schülein, E., Knight, D., Thivet, F., Gaitonde, D., and Schmisser, J., “Experimental and Computational Studies of Crossing-Shock-Wave/Turbulent Boundary-Layer Interactions”, in Proceedings of the International Conference on Recent Developments in Applied Mathematics and Mechanics: Theory, Experiment, and Practice – Devoted to N. N. Yanenko's 80th Anniversary, *Computational Technologies*, Special Issue on CDROM, ISSN 1560-7534, Editor-in Chief Academician Y. Shokin, Vol. 6, Part 2, 2001, 10 pp.

⁸³Knight, D., Gnedin, M., Becht, R., and Zhel'tovodov, A., “Numerical Simulation of Crossing-Shock-Wave/Turbulent Boundary-Layer Interaction Using a Two-Equation Model of Turbulence”, *Journal of Fluid Mechanics*, Vol. 409, 2000, pp. 121–147.

⁸⁴Thivet, F., Knight, D., Zhel'tovodov, A., and Maksimov, A., “Some Insights in Turbulence Modeling for Crossing-Shock-Wave/Boundary-Layer Interactions”, AIAA Paper No. 2000-0131, 2000.

⁸⁵Thivet, F., Knight, D., and Zhel'tovodov, A., “Computation of Crossing-Shock-Wave / Boundary Layer Interaction with Realizable Two-Equation Turbulence Models”, Proceedings of

the International Conference on the Methods of Aerophysical Research, Part 1, Novosibirsk, 2000, pp. 195-201.

⁸⁶Zheltovodov, A., Maksimov, A., Schülein, E., Gaitonde, D., and Schmisser, J., "Verification of Crossing-Shock-Wave / Boundary Layer Interaction Computations with the k-e Turbulence Model", Proceedings of the International Conference on the Methods of Aerophysical Research, Part 1, Novosibirsk, 2000, pp. 231-241.

⁸⁷Zheltovodov, A., Maksimov, A., Gaitonde, D., Visbal M., and Shang J., "Experimental and Numerical Study of Symmetric Interaction of Crossing Shocks and Expansion Waves with a Turbulent Boundary Layer", *Thermophysics and Aeromechanics*, Vol. 7, No. 2, 2000, pp. 155-171.

⁸⁸Schmisser, J., Gaitonde, D., Zheltovodov, A., "Exploration of 3-D Shock Turbulent Boundary Layer Interactions Through Combined Experimental/Computational Analysis", AIAA Paper No. 2000-2378, 2000.

⁸⁹Gaitonde, D., Shang J., Garrison T., Zheltovodov, A., and Maksimov, A., "Three-Dimensional Turbulent Interactions Caused by Asymmetric Crossing-Shock Configurations", *AIAA Journal*, Vol. 37, No. 12, 1999, pp. 1602-1608.

⁹⁰Gaitonde, D., Visbal, M., Shang, J., Zheltovodov, A., and Maksimov, A., "Parametric Investigation of Flowfield Structure and Validation Issues in 3-D Crossing-Shock Wave/Turbulent Boundary Layer Interactions", Proceedings of the International Conference on the Methods of Aerophysical Research, Part 1, Novosibirsk, 1998, pp. 67-76.

⁹¹Gaitonde, D., Shang J., Garrison T., Zheltovodov, A., and Maksimov, A., "Evolution of the Separated Flowfield in a 3-D Shock Wave/Turbulent Boundary Layer Interaction", AIAA Paper No. 97-1837, 1997.

⁹²Shumann, U., "Realizability of Reynolds Stress Turbulence Models", *Physics of Fluids*, Vol. 20, No. 5, 1977, pp. 721-725.

⁹³Coakley, T., and Huang, P., "Turbulence Modeling for High Speed Flows", AIAA Paper No. 92-0436, 1992.

⁹⁴Zeman, O., "Dilatation Dissipation: The Concept and Application in Modeling Compressible Mixing Layers", *Physics of Fluids*, Vol. 2, No. 2, 1990, pp. 178-188.

⁹⁵Sarkar, S., Erlebacher, G., Hussaini, M., and Kreiss, O., "The Analysis and Modeling of Dilatational Terms in Compressible Turbulence", *Journal of Fluid Mechanics*, Vol. 227, June 1991, pp. 473-493.

⁹⁶Aupoix, B., Desmet, E., and Viala, S., "Hypersonic Turbulent Boundary Layer Modeling", *Transitional and Turbulent Compressible Flows*, L. Kral and T. Zang (Eds.), FED Vol. 151, American Society of Mechanical Engineers, 1993, pp. 175-182.

⁹⁷Schmisser, J., and Gaitonde, D., "Numerical Investigation of New Topologies in Strong Crossing Shock Wave Turbulent Boundary Layer Interaction", AIAA Paper No. 2000-0931, 2000.

⁹⁸Panaras, A., Private Communication, September 2001.

⁹⁹Schülein, E., and Zheltovodov, A., "Development of Experimental Methods for the Hypersonic Flow Studies in Ludweig Tube", in *Proceedings of the International Conference on the Methods of Aerophysical Research: Part 1*, Institute of Theoretical and Applied Mechanics, Novosibirsk, Russia, 1998, pp. 191-199.

¹⁰⁰Schülein, E., and Zheltovodov, A., "Documentation of Experimental Data for Hypersonic 3-D Shock Waves / Turbulent Boundary Layer Separation", DLR IB 223-99 A 26, Göttingen, 2001, 95 pp.

¹⁰¹Zheltovodov, A., and Maksimov, A., "Hypersonic Crossing Shock Waves Turbulent Boundary Layer Interactions", Final Technical Report, EOARD Contract F61775-98-WE091, Russian Academy of Sciences, Novosibirsk, Russia, 1999.

¹⁰²Jones, W., and Launder, B., "The Prediction of Laminarization with a Two-Equation Model of Turbulence", *International Journal of Heat and Mass Transfer*, Vol. 15, 1972, pp. 301-314.

¹⁰³Launder, B., and Sharma, B., "Application of the Energy Dissipation Model of Turbulence to the Calculation of Flows Near a Spinning Disk", *Letters in Heat and Mass Transfer*, Vol. 1, 1974, pp. 131-138.

¹⁰⁴Panaras, A., Private Communication, June 2001.